Elsevier Editorial System(tm) for Lithos
Manuscript Draft

Manuscript Number:

Title: Calc-alkaline refertilization and alkaline metasomatism in the Eastern Transylvanian Basin lithospheric mantle: evidences from mineral chemistry and noble gases in fluid inclusions

Article Type: VSI:EMAW- Mantle Paradigms

Keywords: MANTLE REFERTILISATION; EASTERN TRANSYLVANIAN BASIN; NOBLE GASES; POST-COLLISIONAL; SUBDUCTION-RELATED METASOMATISM

Corresponding Author: Dr. Barbara Faccini, Ph.D

Corresponding Author's Institution: University of Ferrara

First Author: Barbara Faccini, Ph.D

Order of Authors: Barbara Faccini, Ph.D; Andrea L Rizzo, Ph D; Costanza Bonadiman, Prof; Theodoros Ntaflos, Prof; Ioan Seghedi, Prof; Michel Grégoire, Prof; Giacomo Ferretti, Ph D; Massimo Coltorti, Prof

Abstract: Calc-alkaline and alkaline magmatisms are generally separated in space and/or in time. Eastern Transylvanian Basin in Romania is one of the few places where the alkaline eruptions of Perşani Mts. occurred contemporaneously with the last calc-alkaline activity of the South Harghita volcanic chain. Mantle xenoliths entrained in Perşani Mts. volcanic products have been studied in order to investigate the interaction of metasomatic agents of different magmatic affinities with the mantle wedge. Based on mineral major and trace element and noble gases in fluid inclusions two main events have been recognized. The first is configured as a pervasive, complete re-fertilization of a previously depleted mantle by a calc-alkaline subduction-related melt, causing the restoration of very fertile, amphibole-bearing lithotypes. This is evidenced by the a) modal clinopyroxene up to 21.9 % with Al2O3 contents up to 8.16 wt%, higher than what expected for clinopyroxene in a Primordial Mantle; b) 4He/40Ar* up to 1.2, within the reported range for mantle production; c) 3He/4He in olivine, opx, and cpx of 5.8±0.2 Ra, among the most radiogenic values of European mantle, below the typical MORB mantle (8±1 Ra), reflecting the recycling of crustal material in the local lithosphere. The second event is related to the interaction with an alkaline metasomatic agent similar to the host basalts that caused a later-stage, slight LREE enrichment in pyroxenes and disseminated amphiboles and the precipitation of vein amphiboles with a composition similar to amphiboles megacrystals also found in Perşani deposits. This is further highlighted by the 4He/40Ar* and 3He/4He values found in some opx and cpx, up to 2.5 and 6.6 Ra, respectively, more typical of magmatic fluids.

Calc-alkaline refertilization and alkaline metasomatism in the Eastern Transylvanian Basin lithospheric mantle: evidences from mineral chemistry and noble gases in fluid inclusions

Abstract

Calc-alkaline and alkaline magmatisms are generally separated in space and/or in time. Eastern Transylvanian Basin in Romania is one of the few places where the alkaline eruptions of Perşani Mts. occurred contemporaneously with the last calc-alkaline activity of the South Harghita volcanic chain. Mantle xenoliths entrained in Perşani Mts. volcanic products have been studied in order to investigate the interaction of metasomatic agents of different magmatic affinities with the mantle wedge. Based on mineral major and trace element and noble gases in fluid inclusions two main events have been recognized. The first is configured as a pervasive, complete re-fertilization of a previously depleted mantle by a calc-alkaline subduction-related melt, causing the restoration of very fertile, amphibole-bearing lithotypes. This is evidenced by the a) modal clinopyroxene up to 21.9 % with Al_2O_3 contents up to 8.16 wt%, higher than what expected for clinopyroxene in a Primordial Mantle; b) $^{4}He/^{40}Ar^{*}$ up to 1.2, within the reported range for mantle production; c) $^{3}He/^{4}He$ in olivine, opx, and cpx of 5.8±0.2 Ra, among the most radiogenic values of European mantle, below the typical MORB mantle (8±1 Ra), reflecting the recycling of crustal material in the local lithosphere. The second event is related to the interaction with an alkaline metasomatic agent similar to the host basalts that caused a later-stage, slight LREE enrichment in pyroxenes and disseminated amphiboles and the precipitation of vein amphiboles with a composition similar to amphiboles megacrystals also found in Perşani deposits. This is further highlighted by the $^{4}He/^{40}Ar^{*}$ and $^{3}He/^{4}He$ values found in some opx and cpx, up to 2.5 and 6.6 Ra, respectively, more typical of magmatic fluids.

HIGHLIGHTS

- Two different kinds of metasomatism in Eastern Transylvania lithospheric mantle
- The mantle wedge was refertilized by a calc-alkaline melt
- Refertilization was followed by alkaline metasomatism, forming amphibole veins
- He-Ne-Ar systematics indicate SCLM refertilization by subduction-related melts

Calc-alkaline refertilization and alkaline metasomatism in the Eastern Transylvanian Basin lithospheric mantle: evidences from mineral chemistry and noble gases in fluid inclusions

Barbara Faccini [a], Andrea Luca Rizzo [a,b], Costanza Bonadiman [a], Theodoros Ntaflos [c], Ioan Seghedi [d], Michel Grégoire [e], Giacomo Ferretti [a], Massimo Coltorti [a]

a Dipartimento di Fisica e Scienze della Terra, Università di Ferrara, Italy

b Sezione di Palermo, Istituto Nazionale di Geofisica e Vulcanologia, Palermo, Italy

c Department of Lithospheric Research, University of Vienna, Austria

d Institute of Geodynamics, Romanian Academy, Romania

e GETCNRS-IRD, Université Paul Sabatier, Toulouse, France

Abstract

Calc-alkaline and alkaline magmatisms are generally separated in space and/or in time. Eastern Transylvanian Basin in Romania is one of the few places where the alkaline eruptions of Perşani Mts. occurred contemporaneously with the last calc-alkaline activity of the South Harghita volcanic chain. Mantle xenoliths entrained in Perşani Mts. volcanic products have been studied in order to investigate the interaction of metasomatic agents of different magmatic affinities with the mantle wedge. Based on mineral major and trace element and noble gases in fluid inclusions two main events have been recognized. The first is configured as a pervasive, complete re-fertilization of a previously depleted mantle by a calc-alkaline subduction-related melt, causing the restoration of very fertile, amphibole-bearing lithotypes. This is evidenced by the a) modal clinopyroxene up to 21.9 % with Al_2O_3 contents up to 8.16 wt%, higher than what expected for clinopyroxene in a Primordial Mantle; b) $^{4}He/^{40}Ar^{*}$ up to 1.2, within the reported range for mantle production; c) $^{3}He/^{4}He$ in olivine, opx, and cpx of 5.8±0.2 Ra, among the most radiogenic values of European

mantle, below the typical MORB mantle (8±1 Ra), reflecting the recycling of crustal material in the local lithosphere. The second event is related to the interaction with an alkaline metasomatic agent similar to the host basalts that caused a later-stage, slight LREE enrichment in pyroxenes and disseminated amphiboles and the precipitation of vein amphiboles with a composition similar to amphiboles megacrystals also found in Perşani deposits. This is further highlighted by the $^{4}He/^{40}Ar^{*}$ and $^{3}He/^{4}He$ values found in some opx and cpx, up to 2.5 and 6.6 Ra, respectively, more typical of magmatic fluids.

Keywords: MANTLE REFERTILISATION, EASTERN TRANSYLVANIAN BASIN, NOBLE GASES, POST-COLLISIONAL, SUBDUCTION-RELATED METASOMATISM

1. INTRODUCTION

Xenoliths representing mantle wedge fragments as defined by Arai and Ishimaru (2008) are rarely found in post-collisional, subduction-related geodynamic settings. They have been collected especially in arc volcanics of the western Pacific like Kamchatka, Japan, Philippines, Papua New Guinea, Vanuatu both in rear-arc position or in the frontal volcanoes and allowed to reconstruct dynamics and metasomatic processes occurring in the mantle wedge of large, mature subduction zones (Yoshikawa et al., 2016 and references therein; Bénard et al., 2018 and references therein). Mantle wedge xenoliths are rarer in eastern Pacific and Atlantic subduction systems (e.g. Brandon and Draper, 1996; Parkinson et al., 2003; Faccini et al., 2013). In Europe, the tectonic complexity and peculiar characteristics of the recent subduction zones (Edward and Grasemann, 2009) as well as the unique presence of ultramafic enclaves in alkaline volcanic products makes it more difficult to establish if they come from a subduction context and can thus be representative of the mantle wedge. In some cases, however, a subduction-related metasomatism has been recognized both from

mineral (Coltorti et al., 2007a; Bianchini et al., 2011 and references therein) and fluid inclusion compositions (Martelli et al., 2011 and references therein; Créon et al., 2017 and references therein).

The Pannonian Basin is one of the most promising areas for the investigation of subduction influence on the magma sources. Its evolution, indeed, has been literally defined as "an interplay of subduction and diapiric uprise in the mantle" (Konečný et al., 2002) where landlocked oceanic lithosphere sections foundered (i.e. expire via sinking into the asthenosphere under their own unstable mass, Edward and Grasemann 2009) causing subduction zone arching and retreat via slab roll-back and consequent asthenospheric doming and corner flow. It comprises several districts (Styria Basin and Burgenland, Little and Great Hungarian Planes and Transylvanian Basin), whose complex evolution from Neogene to Quaternary saw the systematic eruption of alkaline and ultrapotassic magmas after the main calc-alkaline volcanic activity (Seghedi and Downes, 2011) within variable time spans (1-10 Ma, Pécskay et al., 1995a, b). This would imply major changes in the magma source that should be reflected in the textural-chemical-petrological characteristics of the upper mantle. Among all xenolith occurrences in the Pannonian Basin, those entrained in the Na-alkaline lavas of Perşani Mts in the Eastern Transylvanian Basin, erupted very close to the youngest calc-alkaline volcanic fields linked to the final stages of subduction along the Carpathian Bend area (Seghedi et al., 2011 and references therein), are the most promising candidates for representing the mantle wedge of a Mediterranean-type subduction zone.

In this paper, we present the results of the petrological and noble gases study of a new suite of mantle xenoliths from Perşani Mts, unveiling the presence of different kinds of metasomatism: one related to the injection of alkaline melts similar to the host magma and another definable as a pervasive refertilization of the mantle domain by calc-alkaline subduction-related melts. Both types of metasomatism are intimately linked to the major geodynamic changes occurred in the area.

2. GEOLOGICAL SETTING

79 The Pliocene–Quaternary Perşani Mountains Volcanic Field (PMVF) is located in the internal part
80 of the Carpathian Bend Area, in the south-eastern corner of the Transylvanian Basin (Fig. 1). It
81 represents the youngest and largest monogenetic volcanic fields in south-eastern Europe. This
82 volcanism was coeval with the last peak of crustal deformation in the Carpathian bending zone
83 (Merten et al., 2010) and the generation of the Braşov Basin (Gîrbacea et al., 1998), as well as with
84 the orogenic adakite-like calc-alkaline volcanism of the southernmost Harghita Mountains, and with
85 the emplacement of two K-alkalic bodies, located 40 km to the east (Szakács et al., 1993; Seghedi et
86 al., 2004, 2011). The PMVF is underlain by a relatively thick continental crust (35–40 km), whereas
87 the thickness of the whole lithosphere is interpreted to be relatively thin (60–80 km; Martin et al.,
88 2006; Seghedi et al., 2011).
89 The volcanic activity occurred in six episodes between 1.2 Ma and 0.6 Ma (Panaiotu et al., 2004,
90 2013), generating 21 monogenetic volcanic centers (maars, tuff-rings, scoria cones and lava flows)
91 in a 22 km long and 8 km wide area (Seghedi et al., 2016). The three contemporaneous magma
92 sources (Na-, K-alkaline, and adakite-like calc-alkaline) detected in a narrow area have been
93 supposed to be facilitated by the same regional tectonic event, coeval with the last episode (latest
94 Pliocene onward) of the tectonic inversion in the Southeastern Carpathians, probably linked to the
95 indentation of the Adria micro-plate (Matenco et al., 2007; Seghedi et al., 2011).
96 The petrological features of the PMVF basalts are similar to those of continental intraplate alkali
97 basalts worldwide (e.g., Lustrino and Wilson, 2007; Harangi et al., 2014), with some subtle
98 differences (e.g. Pb isotopic characteristics, high LILE) resembling those of subduction-related
99 magmas, thus suggesting a generation from a mantle source slightly influenced by subduction
100 components. The frequent occurrence of mantle xenoliths in the PMVF provides evidence for a
101 rapid magma ascent, within only 4-5 days (Harangi et al., 2013). This indicates that the magmas,
102 generated by deep mantle processes, were almost unaffected by interaction with the crust (Vaselli et
103 al., 1995; Downes et al., 1995; Falus et al., 2008; Seghedi et al., 2011; Harangi et al., 2013).
104

3. PETROGRAPHIC OUTLINE

3.1 Sample location and classification

PMVF mantle xenoliths were collected from pyroclastic deposits of La Gruiu and Fântana eruptive centers and from lava flows along Bârc and Trestia creeks (Fig. 1). The xenoliths are fresh, with sizes varying from 4 to 12 cm in diameter. Modal estimates were obtained mainly by thin section point counting; if the samples were large enough to allow whole rock analyses, the point counting results were crosschecked with mass balance calculations between whole rock and mineral major element compositions.

Lherzolite is the most common rock type, with a total of 30 out of 34 samples. The main characteristic is the almost ubiquitous presence of disseminated pargasitic amphibole, texturally equilibrated with the other constituent minerals and whose modal abundance varies between traces and 11.5 %. Two harzburgites (one with amphibole and one anhydrous), an amphibole-bearing olivine-clinopyroxenite and an anhydrous dunite complete the collection. Lherzolite LAG52 displays an amphibole vein.

Detailed observations of microstructures and olivine Crystal Preferred Orientation carried out on several hundred of PMVF mantle xenoliths by Falus et al. (2011) allowed to recognize that PMVF xenoliths recorded deformation by dislocation creep under different ranges of temperature, stress and strain rate conditions. This resulted in a continuous textural gradation from coarse-grained to fine-grained, mylonitic types, these last making up to about 15% of the ultramafic rocks. Such a textural transition is evident in our suites although only one sample is patently mylonitic. Coarse- to medium-grained samples are predominant and can satisfactorily be described on the basis of the petrographic classification of Mercier and Nicolas (1975). Following these considerations, PMVF lherzolites were divided into two main textural groups (Table 1). A detailed petrographic description is provided in ESM1.

3.2 Protogranular group

This group includes all samples matching the protogranular type as described by Mercier and Nicolas (1975). It can be further divided into two sub-groups, on the basis of some peculiar textural features: *Protogranular s.s. (Pr s.s.)* and *Protogranular with small, rounded grains (Pr srg)* (Table 1; ESM1). Both *Pr s.s.* and *Pr srg* find a correspondence to the coarse-grained peridotites described by Falus et al. (2011) who, however, defined them as being porphyroclastic showing such a continuous variation in grain size that the distinction between porphyroclasts and recrystallized grains has been hindered. These kinds of texture would form at high-temperature (as also noted by Chalot-Prat and Boullier, 1997), low-stress conditions like those prevailing at deep levels within the lithosphere and at lithosphere/asthenosphere boundary. We chose to classify them as Protogranular on the basis of their close resemblance to the Mercier and Nicolas (1975) type description, being aware of the fact that no "pristine" un-deformed lithospheric mantle portions are probably preserved anywhere on Earth and all textural types actually are the result of a series of deformation and recrystallization events.

3.3 Porphyroclastic group

This group includes all samples patently porphyroclastic. It is divided into two sub-groups according to some peculiar textural features: *Porphyroclastic with large, rounded grains (Po lrg)* and *Porphyroclastic s.s. (Po s.s.).* (Table 1; ESM1). *Po lrg* and *Po s.s.* find a strict correspondence with intermediate to fine-grained porphyroclastic peridotites described by Falus et al. (2011). This texture would indicate lower temperatures (Chalot-Prat and Boullier, 1997) and higher stress conditions with respect to those endured by the Protogranular group, suggesting that these samples may come from shallower depth, probably the upper levels of the lithospheric mantle.

3.4 Description of the fluid inclusions

Irrespective of textural type, FI are remarkably scarce in PMVF mantle xenoliths and very small in dimensions (only few μm across). As observed in other occurrences of Central Europe (Rizzo et al., 2018 and references therein) and according to the classification of Roedder (1984), FI occur i) as primary inclusions, generally isolated or arranged in short, tiny trails and/or ii) as secondary inclusions, often forming cluster stripes or trails along plans. In PMVF xenoliths, primary FI could not be clearly identified within single, coarse-grained olivine or pyroxenes; in some samples they were totally absent. The few observed FI are secondary inclusions as trails aligned in planes within the same crystal and/or developed along grain boundaries. Trails of secondary inclusions crossing or straddling between two different crystals were not found.

4. ANALYTICAL METHODS

Bulk rock major and the trace elements Ba, Co, Cr, Ga, Ni, Rb, Sc, Sr, V, Zn and Zr were analyzed with the sequential X-ray spectrometer Phillips PW 2400, equipped with a Rh-excitation source, at the Department of Lithospheric Research of the University of Vienna. For the bulk major and trace elements analyzed by XRF, replicate analyses of the geo-standards UB-N and BHVO-1 yielded an overall procedural error better than 2% and 5% respectively.

Mineral major element compositions were determined by combined microscopic and back-scattered electron (BSE) imaging, followed by analysis using a CAMECA SX100 electron microprobe equipped with four WD and one ED spectrometers, at the Department of Lithospheric Research, University of Wien (Austria). The operating conditions were: 15 kV accelerating voltage, 20 nA beam current, 20 s counting time on peak position. Natural and synthetic standards were used for calibration and PAP corrections were applied to the intensity data (Pouchou and Pichoir, 1991).

Trace element concentrations in pyroxenes and amphiboles were obtained by Laser Ablation Microprobe Inductively Coupled Plasma Mass Spectrometry (LAM-ICP-MS) at the IGG (Istituto di Geoscienze e Georisorse) - C.N.R., Pavia (Italy). The basic set and protocol were described by Tiepolo et al. (2003). A 40–80 μm beam diameter was used, depending on mineral phase. NIST 610

and NIST 612 standard glasses were used to calibrate relative element sensitivity. The precision and accuracy of trace element analyses were assessed by standard sample BCR-2 (reference values from USGS Geochemical Reference Materials Database). Each analysis was corrected with internal standards using CaO for clinopyroxene and amphibole and SiO_2 for orthopyroxene. The detection limit is a function of the ablation volume and counting time and was therefore calculated for each analysis; indeed, ablation volume greatly depends on instrument configuration. As a consequence, the detection limit reduces if spot size, beam power and cell gas flow are decreased. Since analyses for clinopyroxenes and amphiboles were carried out using a smaller spot size and lower beam power, the detection limit for some elements was up to two times less than standard analyses. On the whole, the theoretical detection limit ranges from 10 to 20 ppb for REE, Ba, Th, U and Zr and 2 ppm for Ti.

Eleven aliquots of pure, unaltered olivine, orthopyroxene, and clinopyroxene larger than 0.5 mm were handpicked for noble gases analyses (He, Ne, Ar) in FI from the same set of samples selected for the mineral chemistry analyses (LAG1, LAG2, LAG21, LAG24, LAG51, LAG52, BARQ4, TRE1, TRE2, TRE3, TRE4). The amount of handpicked minerals varied from 0.07 to 1.27 g, depending on xenoliths availability and gas released from FI. The crystals were prepared and analyzed at the Istituto Nazionale di Geofisica e Vulcanologia (INGV), Sezione di Palermo (Italy), following the local isotope laboratory protocol reported by Rizzo et al. (2018).

The element and isotope composition of noble gases (He, Ne, and Ar) was determined by loading the mineral aliquots into a six-position stainless-steel crusher. FI were released by in-vacuo single-step crushing at about 200 bar. This procedure is conservative because it minimizes the contribution of cosmogenic ^3He and radiogenic ^4He that could possibly have grown or been trapped in the crystal lattice (Kurz, 1986; Hilton et al., 1993, 2002; Rizzo et al., 2018). However, since our samples were collected in a quarry and are very young, we can exclude any secondary effect that will not be further discussed.

206 The values of the $^{3}He/^{4}He$ ratio are expressed in units of R/Ra, where Ra is the $^{3}He/^{4}He$ ratio of air,
207 which is equal to 1.39×10^{-6}. The analytical uncertainty of the He-isotope ratio (1σ) was between 0.7
208 and 12%, while this was <4% and <4.3% for $^{20}Ne/^{22}Ne$ and $^{21}Ne/^{22}Ne$, respectively (with the
209 exception of one measurement in opx from LAG1 that is 20.3% for $^{21}Ne/^{22}Ne$). The reported values
210 of both Ne-isotope ratios are corrected for isobaric interferences at m/z values of 20 ($^{40}Ar^{2+}$) and 22
211 ($^{44}CO_2^{2+}$) (Rizzo et al., 2018). Ar isotopes (^{36}Ar, ^{38}Ar, and ^{40}Ar) were analyzed with an analytical
212 uncertainty (1σ) <2.4%. Typical blanks for He, Ne, and Ar were $<10^{-15}$, $<10^{-16}$, and $<10^{-14}$ mol,
213 respectively.

214 ^{40}Ar was corrected for air contamination ($^{40}Ar^*$) as follows:

215 $$^{40}Ar^* = {}^{40}Ar_{sample} - [{}^{36}Ar_{sample} \cdot (^{40}Ar/^{36}Ar)_{air}]$$

216 $^{3}He/^{4}He$ was corrected for contamination based on the measured $^{4}He/^{20}Ne$ ratio as follows:

217 $$Rc/Ra = [(R_M/Ra)(He/Ne)_M - (He/Ne)_{air}]/[(He/Ne)_M - (He/Ne)_{air}]$$

218 where subscripts "M" and "air" refer to measured and atmospheric theoretical values, respectively.
219 Hereafter the corrected $^{3}He/^{4}He$ will be reported as Rc/Ra values.

220

221 # 5. WHOLE ROCK AND MINERAL CHEMISTRY

222 ## 5.1 Whole rock major and trace elements

223 Whole rock compositions were determined for the 15 samples, representative of all the recognized
224 textural tpes. Xenoliths belonging to the Protogranular group (*Pr s.s.* and *Pr srg*) have lower MgO
225 (38.4 – 45.8 wt%) and higher SiO_2 (43.9 – 45.3 wt%), TiO_2 (0.11 – 0.17 wt%), Al_2O_3 (3.26 – 4.31
226 wt%) and CaO (2.44 – 4.88 wt%) than those belonging to the Porphyroclastic group (*Po s.s.* and *Po*
227 *lrg*; MgO, 41.8 – 45.8 wt%; SiO_2, 43.5 – 44.7 wt%; TiO_2, 0.06 - 0.14 wt%; Al_2O_3, 2.05 – 3.26 wt%;

CaO, 1.03 – 2.44 wt%). Na_2O (< 0.42 wt%) and FeOtot (6.77 – 8.17 wt%,) are similar in both Groups, with only one sample with FeOtot content as high as 9.33 wt%.

Ni, Cr and Co contents are very similar for all textural types (1829 - 2244 ppm, 1882 - 3444 ppm and 105 – 115 ppm, respectively) while Zr and V tend to be lower in Porphyroclastic (2.7 – 7.7 and 40.6 – 63.5 ppm, respectively) than in Protogranular group (4.4 – 9.7 and 61.2 – 78.5 ppm, respectively). No difference was envisaged between amphibole-bearing and anhydrous samples, although the latter are too scarce to be statistically representative.

5.2 Mineral major elements

5.2.1 Olivine

Irrespective of the textural group, primary olivine has forsteritic component (Fo) ranging from 88.9 to 91.8 (Table 1; ESM2-1), the lowest values belonging to grains close to the amphibole vein of lherzolite LAG52, while the highest being recorded in the large porphyroclasts of anhydrous harzburgite TRE1. The NiO varies from 0.34 to 0.43 wt% and have no correlation with Fo nor with textural group. According to Herzberg et al. (2016), such high NiO is typical of depleted lithologies, although Straub et al. (2011) found akin contents for olivine in equilibrium with basaltic melts. Idiomorphic secondary olivine in veins and glassy patches are characterized by higher Fo (90.7 – 94.1) and lower NiO contents (down to 0.15 wt%) than those of primary olivine.

5.2.2 Clinopyroxene

Primary clinopyroxene (cpx) exhibit a large range of mg# (89.0 - 92.9) and Al_2O_3 (3.27 -8.16 wt%) (Fig. 2A; ESM2-1). Cpx of *Pr s.s.*, *Pr srg* and *Po lrg* sub-groups are more fertile than those in *Po s.s* sub-group. This is in agreement with Szabó et al. (1995a), who also noticed higher basaltic components in the less deformed xenoliths. In composite sample TRE4, cpx in the clinopyroxenitic portion have lower mg# and higher Al_2O_3 than cpx in the peridotitic matrix (Fig. 2A). TiO_2 is always lower than 0.71 wt%, with the lowest values found in cpx of anhydrous harzburgite TRE1

254 (Fig. 2B). As already noticed by Falus et al. (2008), a positive correlation between Al_2O_3 and Na_2O
255 is observed, with *Po s.s.* and *Pr s.s.* falling respectively at the lowest and highest trend ends (Fig.
256 2C).
257 Secondary cpx can be divided into three types based on mg# and Al_2O_3 contents (Fig. 2D). Type 1
258 are found around amphibole close to glassy patches whereas type 2 includes small idiomorphic cpx
259 in glassy patches and rims of spongy primary pyroxenes. Type 1 have equal to lower mg# at
260 increasing Al_2O_3 values with respect to their associated primary cpx, while type 2 have higher mg#
261 at similar or lower Al_2O_3 contents. Type 3 can be observed only as crystallites in host basalt veinlets
262 and are characterized by a sharp decrease in mg# and an increase in Al_2O_3 with respect to primary
263 cpx. All three types of secondary cpx generally have higher TiO_2 and Cr_2O_3 and equal or lower CaO
264 and Na_2O contents with respect to their primary counterpart.
265
266 ***5.2.3 Orthopyroxene***
267 Orthopyroxene (opx) have mg# varying from 89.1 to 92.1(Fig. 3A, ESM2-1). Analogously to
268 olivine, the lower values characterize opx close to the amphibole vein in LAG52 while the highest
269 values are recorded by anhydrous harzburgite TRE1. TRE1 opx also have the lowest Al_2O_3 contents
270 (2.84 – 3.62 wt%) of the entire PMVF xenolith suite (2.84 – 5.90 wt%). No remarkable major
271 element compositional difference could be observed between porphyroclasts and neoblasts.
272 However, in contrast with what stated by Szabó et al. (1995a), Vaselli et al. (1995) and Falus et al.
273 (2008), a slight difference in geochemical composition coupled with textural variations can be
274 detected. Ca indeed allows a good discrimination between the textural groups, with Protogranular
275 types having higher CaO contents than Porphyroclastic types (Fig. 3B).
276
277 ***5.2.4 Amphibole***
278 Disseminated amphiboles are the overall dominant textural type in the PMVF mantle xenoliths.
279 While several vein amphiboles have been previously found and described within PMVF ultramafic

xenoliths (Vaselli et al., 1995; Zanetti et al., 1995), only the vein of sample LAG 52 can be compared to those described in the literature.

Disseminated amphibole mg# spans from 86.8 (LAG52) to 89.5 (TRE2) (Fig. 4A; ESM2-1); amphibole from *Pr s.s.*, *Pr srg* and *Po lrg* are rather constant in composition within the same sample, with Al_2O_3 contents in the narrow range of 15.3 - 16.3 wt%, while those of the composite sample TRE4 (*Po s.s.*) goes from 14.6 to 16.2 wt%, the higher variability being recorded in the clinopyroxenitic portion. On the whole, Al_2O_3 contents are among the highest for calcic amphibole in European mantle xenoliths (Styrian Basin, Coltorti et al., 2007a; Massif Central, Touron et al., 2008; Eifel, Witt-Eickshen et al., 1998; Balaton, Szabó et al., 1995; Zanetti et al., 1995, Bali et al., 2002; Ntaflos et al., 2017 and Tallante, Coltorti et al., 2007b) and, more broadly, in mantle xenoliths occurring in both intraplate (for example Ionov and Hofmann 1995; Lee et al., 2000; Moine et al., 2001; Ionov et al., 2002) and suprasubduction (for example Kepezhinskas et al., 1996; Abe et al., 1998; Grégoire et al., 2001; Franz et al., 2002; Ishimaru and Arai 2008; Yoshikawa et al., 2016) geodynamic settings, at comparable mg# (ESM3-1). CaO in amphiboles of *Pr s.s.*, *Pr srg* and *Po lrg* textural sub-groups is lower with respect to those of the *Po s.s.* sub-group. The abundance of transition elements such as Cr_2O_3 and TiO_2 has no link to textural type while Na_2O and K_2O respectively show mild positive and negative correlations with mg#.

Amphibole vein of LAG52 is characterized by the lowest mg# and the highest K_2O. Its Na_2O, Al_2O_3 and Cr_2O_3 are lower and TiO_2 is higher (Fig. 4B) with respect to disseminated amphibole in the same sample. A continuous variation between LAG52 vein amphibole, the veins analyzed by Vaselli et al. (1995) and PMVF pargasitic to kaersutitic amphibole MXC (Downes et al., 1995; Zanetti et al., 1995; Demény et al., 2005) can be observed (Fig. 4B). This behavior confirms the findings of Vaselli et al. (1995) (in their Fig. 4) but it has to be underlined that a gap in the trends between disseminated amphiboles and vein amphiboles and selvages is always present for mg#, alkalis and Cr_2O_3.

306 ***5.2.5 Spinel***

307 All samples host primary spinel and the few secondary spinel do not show remarkable chemical
308 differences. For sake of clarity, we describe the primary spinel only.

309 They are Al-rich (Table1; ESM2-1), with very low cr# (6.64 - 16.0) but high mg# (74.8 – 79.19),
310 comparable to that of abyssal peridotite spinel (Shibata and Thompson, 1986; Dick, 1989; Bonatti
311 et al., 1992, 1993; Dick and Natland, 1996; Seyler et al., 2003; Schmädicke et al., 2011). Al-rich
312 spinel associated to LAG52 vein amphiboles are also relatively iron rich (mg# 70.6 – 71.4), whereas
313 primary spinel of the anhydrous harzburgite TRE1 are clearly distinct, having comparable mg#
314 (71.8-74.6) but the highest cr# (28.6-34.6) values of the entire xenolith population. (Fig. 5) In the
315 Olivine-Spinel Mantle Array (OSMA, ESM3-2) all spinel fall in the lower end of the continental
316 peridotites field, with the only exception of TRE1.

317

318 ## 5.3 Mineral trace elements

319 Pyroxenes and amphiboles were measured with an average of 5 spots *per* sample. Within the single
320 nodule, trace element content of each phase resulted very homogeneous, with almost no variations
321 between cores and rims. For this reason, the mean concentration of each element was calculated, for
322 most of the minerals, in all samples (ESM2-2). This reduced dataset was used for modeling. On the
323 basis of chondrite-normalized REE patterns, pyroxenes have been divided into three groups.

324

325 ***5.3.1 Clinopyroxenes***

326 Cpx in each sample generally fall within a single group but samples BARQ4 and TRE4 have cpx
327 belonging to two groups.

328 Group 1 (including BARQ4, LAG21, LAG24 and TRE4) is represented by cpx characterized by
329 slightly Light (LREE) to Middle (MREE) rare earth element convex-upward depleted patterns (Fig.
330 6A), with $(La/Yb)_N$ spanning from 0.34 to 0.48. The smooth convexity of the pattern can be
331 measured by $(Eu/Yb)_N$, varying between 0.92 to 1.54 (average 1.24). In this Group, Heavy rare

earth element (HREE) contents are slightly variable, with $(Yb)_N$ ranging from 9.35 to 13.3. In Chondrite-normalized trace element diagrams (Fig. 6B), they show variable degrees of enrichments in Th and U (up to 8.34 and 37.4, respectively) and a ubiquitous Ti negative anomaly; Zr and Hf can be decoupled.

Group 2 (including BARQ4, LAG1, TRE2 and TRE4), at the first glance, has mostly the same REE profile of Group 1 but it actually has flatter M to HREE [$(Eu/Yb)_N$ = 0.71 - 1.11; average 0.94)], highly variable HREE contents [$(Yb)_N$, 8.83 - 19.0)] and slight enrichments in La and Ce [$(La/Yb)_N$ = 0.16 - 0.74)] (Fig. 6C). In chondrite normalized trace element patterns Group 2 cpx are similar to those of Group 1 but for a slight Sr positive anomaly (Fig. 6D).

Group 3 (including LAG51, LAG52 and TRE1) is the most LREE enriched (Fig. 6E), with the highest $(La/Yb)_N$ ratios of the whole suite (1.42 – 2.57) and spoon-shaped REE patterns. These cpx also have the highest Th and U contents, up to 48 and 102 x Chondrite, respectively (Fig. 6F). HREE are comparable to those of the other Groups [$(Yb)_N$, 8.94 – 12.6]. This Group includes cpx of anhydrous harzburgite TRE1, showing the same REE profile with the lowest M-HREE contents.

There is no neat correspondence between the types recognized from texture and major elements and cpx Groups according to their trace element inventory. It can be noted that cpx modal content increases in the sequence Group 3 - Group 1 – Group 2 (Table 1).

5.3.2 Orthopyroxenes

For all PMVF lherzolites, opx Chondrite-normalized trace element patterns are characterized by steep REE patterns and positive Zr-Hf and Ti anomalies (Fig. 7). Opx associated to Group 1 cpx are the most depleted (beside a slight La enrichment) (Fig. 7A), with ubiquitous Sr negative anomaly {Sr*= Sr/[(Sm+Nd)/2], 0.15 – 0.42} and low Th contents (up to 0.34 x Chondrite) (Fig. 7B). Group 2 opx show LREE enrichments concordant with those of the associated cpx (Fig. 7C); they largely overlap opx of Group 1 with higher Th (up to 3.12 x Chondrite) and less pronounced Sr negative anomalies (Sr*, 0.28 – 1.02) (Fig. 7D). Opx associated with Group 3 cpx show an overall La to Tb

358 enrichment (Fig. 7E) and the highest Th contents (up to 3.72 x Chondrite) but have similar Sr* to
359 that of Group 2 opx (0.45 – 0.47) (Fig. 7F).
360
361 ***5.3.3 Amphiboles***
362 Chondrite-normalized trace element and REE patterns of disseminated amphibole mimic very well
363 those of the coexisting cpx (Fig. 8) in each sample and, on average, for each Group.
364 Group 1 amphiboles have the most depleted [$(La/Yb)_N$, 0.26 – 0.48], well-defined convex upward
365 REE patterns [$(Eu/Yb)_N$, 0.94 – 1.36] (Fig. 8A); they show either Nb-Ta positive or negative
366 anomalies (Fig. 8B) even though their contents are low (Nb, up to 3.04 ppm; Ta, up to 0.21 ppm).
367 Positive Nb-Ta anomalies are always associated with negative Th-U anomalies and *vice versa*, thus
368 the higher Th and U values (up to 6.34 and 17 x Chondrite, respectively) are reached in amphiboles
369 with the lowest Nb contents. Group 1 is also characterized by the most pronounced Ti positive
370 anomalies (Ti* = Ti/[(Eu+Gd)/2], 0.9 – 2.3; average 1.6).
371 Group 2 includes amphiboles showing slight La and Ce enrichments [$(La/Yb)_N$, 0.33 – 0.83] and
372 less convex REE pattern [$(Eu/Yb)_N$, 0.5 – 1.21] with respect to Group 1 amphiboles (Fig. 8C). The
373 opposite behavior between Nb-Ta and Th-U anomalies persists (Fig. 8D), with similar Nb and Ta
374 contents (Nb, up to 3.61 ppm; Ta, 0.28 ppm, respectively) and a slight increase of Th spike (13.6 x
375 Chondrite). Ti negative anomaly tend to reduce in this Group (Ti*, 0.9 – 2.1, average 1.4).
376 Amphiboles falling within Group 3 are remarkably enriched in LREE [$(La/Yb)_N$, 1.37 – 2.17] with
377 respect to the previous groups, forming smooth spoon-shaped patterns (Fig. 8E). They have Th and
378 U values similar to those of the other groups (up to 16.9 and 15, respectively) but reach the highest
379 Nb contents (63 x Chondrite) among disseminated amphiboles (Fig. 8F).
380 Amphibole vein in sample LAG52 is included in Group 3 and is shown as a single average (Fig.
381 8E,F) due to the similarity between the various analyzed spots. It is characterized by a pronounced
382 REE fractionated pattern with L-MREE enrichments [$(La/Yb)_N$, 4], the highest HFSE contents
383 [$(Nb)_N$, 150 x Chondrite; $(Zr)_N$, 92 x Chondrite; $(Hf)_N$, 2.7 x Chondrite] and a feeble negative Ti

anomaly (Ti*, 0.7). Its pattern fit well those of amphibole veins found in both PMVF peridotites and clinopyroxenites by Zanetti et al. (1995), Vaselli et al. (1995) and Chalot-Prat and Bouillier (1997) (ESM3-3). Like for major elements, trace element budget of these veins also show many similarities with amphibole MXC (ESM3-3, Zanetti et al., 1995; Downes et al., 1995) which, however, are on average characterized by slightly lower LREE and a remarkable Ti positive anomaly (Ti*, 1.71 – 4.08).

5.4 Noble gas elemental and isotopic compositions

Olivine systematically show the lowest concentration of ^{4}He and $^{40}Ar^{*}$, while cpx and opx have a comparable range of values (ESM3-4). The highest concentration for the three minerals is found in LAG52 that also shows the lowest mg# (see Section 5.2). ^{4}He is positively correlated with $^{40}Ar^{*}$, indicating that ^{4}He-rich FI are also $^{40}Ar^{*}$-rich and, reasonably, rich in the other gas species.

The $^{4}He/^{20}Ne$ ratio is 0.7-41.7 in ol, 11–1960 in opx, and 8.3–1394 in cpx (ESM2-3). The $^{40}Ar/^{36}Ar$ ratio is 286–326 in ol, 350–879 in opx, and 319–1867 in cpx (ESM2-3). The $^{20}Ne/^{22}Ne$ and $^{21}Ne/^{22}Ne$ ratios are 9.8–10.0 and 0.0283–0.0327, respectively, in olivine, 9.8–10.1 and 0.0291–0.0342 in opx, and 9.9–10.1 and 0.0290–0.346 in cpx (ESM2-3 and Fig. 9).

The $^{3}He/^{4}He$ ratio corrected for air contamination (Rc/Ra value) is 1.5–5.9 Ra in olivine, 5.4–6.8 Ra in opx, and 2.2–6.8 Ra in cpx (ESM2-3 and Fig. 10). The highest $^{3}He/^{4}He$ values within olivine were measured in LAG52 and TRE2 (5.4 and 5.9 Ra, respectively), and only in the case of LAG52 it corresponds to the highest concentration of ^{4}He (94 $\times 10^{-14}$ mol/g) and $^{40}Ar^{*}$ (42$\times 10^{-14}$ mol/g) (Fig. Z). At progressively lower concentration of ^{4}He and $^{40}Ar^{*}$, $^{3}He/^{4}He$ values decrease. The highest $^{3}He/^{4}He$ ratios in opx and cpx are measured in TRE1 and TRE2 (Fig. 10; ESM2-3).

6 DISCUSSION

6.1 Mineral equilibrium and temperature estimation

409 The Mg and Fe equilibrium exchange (Brey and Köhler, 1990) among peridotite minerals allows
410 evaluating how much mineral pairs match equilibrium, coherently with their Fe/Mg distribution.
411 Irrespective of textural type and amphibole modal percentage, the Fe/Mg exchange between olivine
412 and opx of PMVF samples reproduces, within the experimental error, the slope of olivine-opx lines
413 calculated for temperatures varying between 927 and 727 °C (1300 - 1100 °K) in the pressure range
414 of 1.5 - 2.0 GPa, (Brey and Köhler, 1990). Olivine-cpx and opx-cpx pairs, distinguished by textural
415 types, also reflect ideal Fe/Mg equilibrium (Brey and Köhler, 1990) in the same temperature and
416 pressure ranges. Minerals in close proximity to host basalts veinlets, showing destabilization due to
417 local thermal effects, were discarded.
418 Equilibrium between olivine and spinel was also evaluated, by comparing the Fe/Mg distribution
419 among the coexisting minerals with the ideal equilibrium distribution of Fe^{2+} and Mg between
420 olivine and the aluminum component in (Mg-Fe)–bearing spinel end members (i.e. spinel s.s. and
421 hercynite, Jamieson and Roeder, 1984). Spinel end-members were calculated assuming that all Ti
422 and Fe^{3+} (as determined by stoichiometry) form ulvöspinel and magnetite components, respectively.
423 Taking into account the diffusion corrections (Lehmann, 1983), Fe-Mg distribution coefficient
424 between olivine and Al-spinel is estimated in the range of 0.90 - 1.23 (Jamieson and Roeder, 1984)
425 at T= 1000-1200 °C.
426 The relevant presence of disseminated amphibole (generally less than 4% but up to 11.5 wt% in one
427 case, Table 1; ESM1) in PMVF peridotites cannot be ignored, discussing the potential intra-mineral
428 equilibrium conditions. Experimentally determined Fe-Mg distribution coefficient ($Kd_{Fe\text{-}Mg}^{cpx\text{-}amph}$)
429 between cpx and amphibole in basanite melts is (on average) 0.76 $\pm$ 0.21 (Hawthorne and Oberti
430 2007; Pilet et al., 2010). This value is also constrained by Ca contents and the subsolidus
431 equilibrium between the two minerals is resolved with [Ca/(Ca+Mg+Fetot)] ~ 1.6 (Forshaw et al.
432 2019), a condition fully satisfied by amphibole/cpx pairs in PMVF peridotitic xenoliths.
433 In the light of these findings, temperature estimations have been carried out using the two pyroxene
434 equations of Brey and Köhler (1990) and Taylor (1988) (Table 1). Brey and Köhler (1990)

435 geothermometer yielded temperatures spanning from 843 to 1056 °C at 2.0 GPa, with standard
436 deviations for each sample (from ±0.7 to ±14) lower than the methodological error (±24°C). Taylor
437 (1998) formula gave comparable results (858-1009 °C at 2.0 GPa), with differences between the
438 two methods always lower than 60°C. Regardless the geothermometers used, *Po s.s.* always
439 recorded temperatures between 111 and 148 °C lower, on average, than the other three textural sub-
440 groups. It has to be noted that *Po lrg* are intermediate between the Protogranular group and *Po s.s*,
441 suggesting a decrease in temperature at increasing "porphyroclastic degree" in PMVF samples, in
442 agreement with the results of Falus et al. (2008) and what has been observed for other mantle
443 xenolith suites from the Pannonian Basin (Embey-Isztin et al., 2001; Ntaflos et al., 2017).
444
445 ## 6.2 Oxygen fugacity and pressure conditions
446 Assuming that thermodynamic parameters are known and activity/composition relations can be
447 assessed, oxygen fugacity (fO_2) in mantle peridotites may be calculated from the heterogeneous
448 redox equilibria:
449 Fayalite (olivine) + O_2 (fluid) = Ferrosilite (opx) + Magnetite (spinel).
450 The calculation is hampered by uncertainties in the activity/composition relations of magnetite
451 component in spinel (Mattioli and Wood, 1988; Wood and Virgo, 1989). Since magnetite solid
452 solution is low in mantle spinel (≤ 2.5% in this xenolith population), typical analytical errors
453 translate into considerable fO_2 uncertainties. We applied the semi-empirical equation of Ballhaus et
454 al. (1991), using the magnetite composition/activity model of Wood and Virgo (1989). The fO_2
455 calculated in terms of divergence from the fayalite-magnetite-quartz (FMQ) buffer are in the
456 restricted range of -1.22 - +0.34, with the lowest values belonging to the *Po s.s.* anhydrous
457 harzburgite TRE1 (Table 1; ESM3-5). These values are comparable to those typical for both off-
458 craton Sub-Continental Lithospheric Mantle (SCLM) and supra-subduction zones (Foley, 2011;
459 Bénard et al., 2018) and to those calculated for Pannonian Basin mantle xenoliths by Szabó et al.
460 (1995b). A vague positive correlation between fO_2 and the modal percentage of the redox sensitive

phase amphibole have been observed; such a correlation seems to be in agreement with the result of Sorbadere et al. (2018) who observed an increase in oxygen fugacity with the increase of H_2O content in a peridotitic system, but was not observed in other cases of amphibole-bearing mantle xenolith populations (Bonadiman et al., 2014).

The pressure of amphibole formation could be tentatively estimated. Recently, Mandler and Grove (2016) made a series of experiments to quantify the effects of pressure, temperature, bulk composition and H_2O content on the stability of amphibole in the Earth's mantle. They established that alkali content of amphibole is a linear function of pressure and temperature and less dependent on bulk compositional variations and water contents, allowing to formulate an empirical thermobarometer for pargasite-bearing garnet (and spinel) peridotites. To avoid circular reference, we introduced in the eq. 1 of Mandler and Grove (2016) the temperatures calculated from Brey and Köhler (1990) geothermometer. According to the Mandler and Grove (2016) equation, PMVF amphibole-bearing lherzolites equilibrated between 2.5 and 2.7 GPa (Table 1), which seem rather high pressures as no garnet is present in their mineral assemblage. These rocks have bulk Cr_2O_3/Al_2O_3 ratios (0.09-0.14) comparable to the experimental fertile hydrous (H_2O= 0.65wt%) lherzolite (0.10), in which the spinel–garnet transition occurs below 2.5 GPa. Taking into account the experimental error and the different water content between natural and experimental lherzolites, the pressure prediction for PMVF amphibole equilibration are therefore consistent with these samples having last equilibrated in the upper pressure limit of the spinel stability field (O'Neill 1981; Klemme 2007; Ziberna et al. 2013). Consequently, a rather deep origin of PMVF mantle xenoliths cannot be discarded. The opx-cpx-spinel clusters found within some samples could be symptomatic of a former garnet as suggested by Falus et al. (2000), which hypothesized a mantle domain moving from a garnet bearing region at pressures higher than 3.0 GPa to a shallower level (1.9 - 2.1 GPa), inferring an upwelling of the PMVF mantle section of 40-60 km. This occurred in the frame of a highly arcuate subduction zone, where rapid tectonic changes were strictly correlated to accelerated slab steepening (Edward and Grasemann, 2009), asthenospheric uprise (Mason et al.,

1998; Harangi, 2001; Seghedi et al., 2004; Kovács et al., 2018) in a post-collisional stage and regional stress redistribution (Seghedi et al., 2011 and references therein).

6.3 Processes that modify the geochemistry of FI

6.3.1 Atmospheric contamination

FI isotope composition of Ne and Ar and, complementarily, the $^{4}He/^{20}Ne$ ratio in PMVF xenoliths highlights a variable air contamination (Fig. 12, ESM2-3), which progressively decreases from olivine to cpx, probably due to the increasing concentration of He-Ne-Ar trapped in FI of the pyroxenes. This is clearly shown by the three Ne isotopes plot (Fig. 9), in which our data fall along or slightly below the theoretical mixing line between air and a MORB-like mantle, defined by Sarda et al. (1988) and Moreira et al. (1998) at $^{21}Ne/^{22}Ne = 0.06$ and $^{20}Ne/^{22}Ne = 12.5$. A similar indication comes from the $^{40}Ar/^{36}Ar$ and $^{3}He/^{36}Ar$ values (Fig. 11), which are well below the theoretical ratio in the mantle ($^{40}Ar/^{36}Ar$ up to 44,000 and $^{3}He/^{36}Ar$~0.45; e.g., Burnard et al., 1997; Moreira et al., 1998; Ballentine et al., 2005), and fall along the binary mixing between air and a MORB-like mantle.

The presence of atmospheric contamination in FI also regards other European SCLM xenoliths [Eifel (Germany) and Massif Central (France), Gautheron et al., 2005; Calatrava and Tallante (Spain), Martelli et al., 2011 (not shown in Fig. 11); Lower Silesia (NE Eger Rift, SW Poland), Rizzo et al., 2018]. For sake of homogeneity, we compare our data with those from other mantle xenoliths locations that were analyzed by single-step crushing and for which $^{40}Ar/^{36}Ar$ data are available. Data from Eifel and Lower Silesia are slightly out from this binary mixing due to different $^{4}He/^{40}Ar^{*}$ and $^{3}He/^{4}He$ ratios (Fig. 12), probably related to distinct mantle features and processes occurred therein (see Sections 6.4 and 6.5). Beside this, mantle xenoliths from PMVF (this study), Calatrava and Tallante show the highest air contamination at comparable ^{4}He concentrations that are likely proportional to the total FI gas content.

As summarized by Rizzo et al. (2018), air in FI from mantle xenoliths could be linked to i) a direct contamination in the SCLM, ii) a contamination acquired by xenoliths during magma ascent, or iii) a post-eruptive entrapment in mineral micro-cracks. Because Perşani volcanism is partly coeval with the post-collisional calc-alkaline magmatism of the South Harghita Mountains, outcropping only 40 Km eastward (Szakács et al., 1993; Seghedi et al., 2004, 2011, 2016; Lustrino and Wilson, 2007), the first hypothesis is, in our opinion, the most reasonable. This hypothesis could also explain the high air contamination found by Martelli et al (2011) in mantle xenoliths from Tallante, which underwent a metasomatism by subduction-related fluids possibly linked to the Cenozoic Betic subduction, although the authors favour the third hypothesis.

6.3.2 Diffusive fractionation

^{4}He and $^{40}Ar^{*}$ in PMVF xenoliths are systematically lower in olivine than in cpx and opx (ESM3-4), with the former having the narrowest range of $^{4}He/^{40}Ar^{*}$ (1.4-2.7), within the reported range for mantle production ($^{4}He/^{40}Ar^{*}$ = 1–5; Marty, 2012). Opx and cpx vary from 0.3 to 2.1 and 0.3 to 2.5, respectively, including values below the mantle production range (Fig. 12). These evidences would suggest that mantle processes such as partial melting and/or refertilization/metasomatism fundamentally modulate the chemical variability of FI. However, comparing ^{4}He and $^{40}Ar^{*}$ with $^{3}He/^{4}He$ (Fig. 10) we notice that, at concentrations of ^{4}He and $^{40}Ar^{*}$ below ~1.0-2.0×10^{-13} mol/g, $^{3}He/^{4}He$ values decrease. On the contrary, opx and cpx do not show any significant difference in the $^{3}He/^{4}He$ values that could be related to ^{4}He and $^{40}Ar^{*}$ concentrations, except cpx from sample TRE4 that has ^{4}He and $^{40}Ar^{*}$ below ~1.0-2.0×10^{-13} mol/g and a $^{4}He/^{40}Ar^{*}$ value of 2.5 (Figs. 10 and 12). In addition, opx and cpx from sample TRE3 show the lowest $^{3}He/^{4}He$ and $^{4}He/^{40}Ar^{*}$ values.

These differences might be originated from a preferential diffusive loss of ^{4}He and $^{40}Ar^{*}$ (e.g., Burnard et al., 1998; Burnard, 2004; Yamamoto et al., 2009 and references therein), which depends on the diffusion coefficient (D), significantly higher for ^{4}He than for $^{40}Ar^{*}$ (D_{4He}/D_{40Ar} = 3.16 in

538 solid mantle; Burnard, 2004; Yamamoto et al., 2009). In case of diffusive loss of helium, we should
539 also expect that $^{3}He/^{4}He$ fractionates due to the appreciable difference in D_{3He} and D_{4He} among
540 mantle minerals (D_{3He}/D_{4He} = 1.15; Trull and Kurz, 1993; Burnard, 2004; Yamamoto et al., 2009
541 and references therein).
542 In Figs. 10 and 12 we model two possible path of diffusive fractionation of He, $^{40}Ar^{*}$, $^{3}He/^{4}He$, and
543 $^{4}He/^{40}Ar^{*}$ during mantle melting, based on the approach of Burnard et al. (1998), Burnard (2004)
544 and Yamamoto et al. (2009). As starting mantle composition, we assumed $^{4}He = 2.5\times10^{-13}$ mol/g,
545 $^{40}Ar^{*} = 9.0\times10^{-14}$ mol/g, and $^{3}He/^{4}He$ = 5.9 Ra. These values were chosen because, immediately
546 below, a decrease of $^{3}He/^{4}He$ is noticed and the $^{4}He/^{40}Ar^{*}$ ratio was within the reported range for
547 mantle production ($^{4}He/^{40}Ar^{*}$ = 1–5; Marty, 2012). The $^{3}He/^{4}He$ was chosen considering the mean
548 ratio in olivine, opx and cpx among data apparently not modified from this process. For the constant
549 concentration of the element in the magma (called Cf in Yamamoto et al., 2009), we assumed two
550 different concentrations of ^{4}He and $^{40}Ar^{*}$ in order to fit our data and those from the literature (see
551 ESM3-4 and Fig. 12 caption for further explanations).
552 According to our modelling, olivine and cpx from TRE4 and opx and cpx from TRE3 fit the paths
553 of diffusive fractionation. Thus, it is likely that this process modified the noble gases composition
554 of the residual mantle during its melting, but it can be appreciated only in those portions where the
555 concentration of noble gases was low (i.e., ^{4}He and $^{40}Ar^{*}$ below ~$1.0\text{-}2.0\times10^{-13}$ mol/g). A process
556 of diffusive fractionation can also explain the data from Calatrava and Tallante mantle xenoliths
557 with concentrations of ^{4}He and $^{40}Ar^{*}$ below of $1.0\text{-}2.0\times10^{-13}$ mol/g (Fig. 10 and 12), as also argued
558 by Martelli et al. (2011). This concentration thus represents a cut off line below which the data
559 cannot be used for considerations on the residual mantle characteristics. It is worth noting, however,
560 that mantle xenoliths from Eifel, French Massif Central, and Styria Basin with ^{4}He concentration
561 below $1.0\text{-}2.0\times10^{-13}$ mol/g do not show any similar variation, suggesting that diffusive fractionation
562 did not occur in these localities or occurred in different conditions, such as to avoid remarkable
563 modification of the FI composition. We argue that this process probably regards only specific

564 portions of European (and worldwide?) SCLM but we have no further arguments to constraints an
565 aspect that is beyond the scope of this study. As far as PMVF FI compositions are concerned, in the
566 following discussions we focus on data not affected by diffusive fractionation.
567
568 ## 6.4 Melting and refertilization events
569 Modal and whole rock compositions of PMVF mantle xenoliths have been compared to existing
570 melting models for off-craton peridotites, in order to puzzle out the melting history of the sampled
571 lithospheric section. Comparing MgO contents with modal percentage of olivine, opx and cpx
572 (ESM3-6), the trends depicted are concordant with the depletion model trends of Niu et al. (1997),
573 although a tendency towards lower modal olivine and higher cpx can be envisaged. Porphyroclastic
574 group have higher MgO contents with respect to Protogranular group. TiO_2 and Al_2O_3 positive
575 correlation would depend upon melt extraction (Takazawa et al., 2000; Ionov, 2007 and references
576 therein). However, considering our data together with those of Vaselli et al. (1995) (ESM3-7), about
577 two third of the samples fit equilibrium melting paths between 2 and 3 GPa, while the remaining
578 (including the majority of our samples) do not follow any residual evolution line, even considering
579 polybaric decompression melting (Ionov and Hoffmann, 2007 and references therein). With only
580 few exceptions, these samples have less iron with respect to the expected Al_2O_3 content, this latter
581 being even higher with respect to the corresponding MgO predicted by models for any kind of
582 melting evolution (ESM3-7), both at constant and decreasing P (Niu, 2004; Ishimaru et al., 2007).
583 Thus, the extremely Al_2O_3-rich compositions of some PMVF mantle xenoliths do not find an
584 explanation if only partial melting is taken into account.
585 Similar information is given by mineral phase composition. Johnson et al. (1990) proposed the most
586 used, mineral focused model to predict the melting degree for batch and fractional melting, based
587 on cpx REE patterns, while more recently Scott et al. (2016) proposed a similar approach for opx.
588 Bonadiman and Coltorti (2011, 2018) and Upton et al. (2011) attempted to infer the partial melting
589 degree of a mantle lithotype based on major element composition of opx, cpx and spinel. As it is

590 well known, cpx is the most important incompatible trace element repository within an anhydrous
591 peridotite, constraining the overall REE budget. Obviously this is not true when a volatile-bearing
592 phase is present, taking into account that amphibole partitioning coefficients are higher than those
593 of cpx for most incompatible elements (see for example Ionov et al., 1997; Witt-Eickschen and
594 Harte 1994). Disseminated amphibole is almost ubiquitous within the PMVF xenoliths, with trace
595 element patterns perfectly mimicking those of cpx apart for elements which are preferentially
596 incorporated in the amphibole crystal lattice (Figs. 6, 7, 8). The ubiquitous similarity between the
597 trace element patterns of the two minerals - regardless of textural positions or presence of
598 amphibole vein - is a strong indication of disseminated amphibole genesis via cpx hydration,
599 followed by subsolidus re-equilibration. Since amphibole grew over cpx, some differences should
600 be expected between cpx patterns in anhydrous and hydrous parageneses. However, the patterns of
601 cpx from anhydrous lherzolite BARQ4 are perfectly comparable with those of cpx from lherzolites
602 LAG21 and LAG24, having 0.7 and 1% of modal disseminated amphibole, respectively. For this
603 reason, no re-distribution modeling backward from amphibole to cpx has been developed and we
604 assumed that the trace element contents of cpx correspond to the original composition, i.e. should
605 represent a suitable indicator of the partial melting degree. Batch, fractional and incremental (with
606 1% increment for each step) melting modeling were thus developed following the Johnson et al.
607 (1990) equations, using as starting composition the primordial, fertile cpx proposed by Bonadiman
608 et al. (2005) for spinel peridotites. The best fit between model and real cpx was obtained for
609 fractional melting (ESM3-8), although many of the samples (BARQ4, LAG21, LAG24, LAG51,
610 TRE4) have HREE and MREE values higher than those of the primordial cpx, while LREE can be
611 variably enriched or depleted. Cpx from lherzolite LAG52 perfectly overlaps the pattern of
612 primordial cpx, while lherzolites LAG1, TRE1 and TRE2 indicate very low degrees of partial
613 melting, between 1 and 5 %. Thus, according to cpx REE composition, PMVF xenolith represent a
614 very fertile mantle that, however, cannot be explained just invoking low-degree melting processes.
615 This conclusion is further enhanced by checking out the opx. According to the model of Scott et al.,

616 (2016), indeed, opx REE patterns indicate substantially higher degrees of melting (ESM3-9). The
617 comparison has been developed based on HREE (since LREE are highly variable and more prone to
618 be modified by post-melting processes) and taking into account that the model starts from the DMM
619 source by Workman and Hart (2005), already slightly depleted by 2-4 % melt extraction.
620 Protogranular group opx would have been affected by a melting event between 12 and 20%,
621 whereas Porphyroclastic group opx would record a F from 20 to 25%, with TRE1 being the most
622 depleted. Using the approach developed by Bonadiman and Coltorti (2018) in the CMAS-Fe system
623 for pressures varying between 1 to 3 GPa and temperatures between 900 and 1300 °C, (which takes
624 also into account the subsolidus re-equilibration), the opx major element composition indicates
625 rather low degrees of partial melting (mainly < 15%), although the fit with the theoretical curve is
626 rather limited (Fig. 3A). The indication of low degree of melting comes from the high Al_2O_3
627 contents that in some samples (BARQ4, LAG24 and LAG2) is higher than that of a primordial opx.
628 As far as mg# is concerned, some samples shift toward higher values and only one (LAG52, the
629 sole with an amphibole vein) towards lower values with respect to the theoretical curve at constant
630 Al_2O_3 value. Taking into account the existing Fe and Mg equilibrium between opx and olivine, as
631 well as the Fo and NiO content of the latter - unlikely for low degree of melting - it can be
632 hypothesized that Al_2O_3 has been added to the system after the partial melting. If this is the case and
633 the opx composition is reported on the curve following the mg#, the obtained degrees of F appear
634 well comparable with those estimated by the HREE in opx. A support to this line of reasoning
635 comes from the composition of primary (and secondary) opx in xenoliths representative of the
636 mantle wedges, entrained in calc-alkaline lavas from Kamchatka (Kepezhinskas et al., 1996; Bryant
637 et al., 2007; Ishimaru et al., 2007; Ionov, 2010; Ionov et al., 2013) and Philippines (Arai et al.,
638 2004; Yoshikawa et al., 2016) (Fig. 3A). These opx match quite well the theoretical line and have
639 high mg# - similar to those of TRE1 – coupled with very low Al_2O_3 contents. It is then reasonable
640 to put forward that PMVF xenoliths were residua of partial melting degrees comparable to those of
641 typical sub-arc mantle that were successively affected by an Al_2O_3 enrichment. The event would

642 have also increased the modal percentage of opx, considering that some PMVF xenoliths have a
643 paragenesis moving toward ol-websterites, with opx modal contents up to 36.2%, much higher than
644 that of a primordial, fertile mantle (25%, Johnson et al., 1990). A SiO_2-saturated, Al_2O_3-rich
645 metasomatizing melt could increase the opx modal content with mg# buffered by the matrix,
646 concomitantly with, or followed by, a textural re-equilibration and re-crystallization. This
647 reorganization could have occurred under the stress regime consequent to slab steepening/sinking
648 and to asthenosphere uprise, that pushed upward the overlying lithospheric mantle column (Falus et
649 al., 2000, 2008, 2011). Enhanced recrystallization of newly formed ("secondary") opx in a mantle
650 wedge can completely delete its initial replacement texture so that it looks like a primary phase
651 (Arai and Ishimaru, 2008).
652 A similar interpretation can be put forward for cpx major elements, having mg# values compatible
653 with melting degrees $\geq$ 25%, but showing Al_2O_3 contents higher than those expected by theoretical
654 calculations. Thus their Mg and Fe contents, being buffered by the matrix, can be considered as
655 good indicators of the partial melting degree, while Al_2O_3 and REE can be related to the enrichment
656 process. As for opx, in Fig. 2A the composition of cpx from various subarc settings, such as
657 Kamchatka (Kepezhinskas et al., 1996; Bryant et al., 2007; Ishimaru et al., 2007; Ionov, 2010),
658 Philippines (Arai et al., 2003, 2004; Yoshikawa et al., 2016), Japan (Abe et al., 1998), Cascade
659 Range (Brandon and Draper, 1996) and Lihir (McInnes et al., 2001) is reported. In all cases, cpx
660 with mg# equal or exceeding the degree of partial melting after which cpx is exhausted (F= 22-
661 25%, Hellebrand et al., 2001; Bernstein et al., 2007; Sobardere et al., 2018) are found, but they
662 show a remarkable Al_2O_3 enrichment with respect to the theoretical curve. It is likely that these cpx
663 were newly formed, growing over a strongly depleted opx in an originally harzburgitic matrix
664 (which buffered the mg#) from an Al_2O_3-rich melt. Alternatively, cpx could have been generated by
665 exsolution from opx and successively texturally re-organized and enriched by an Al_2O_3-rich
666 metasomatizing melt. In the Protogranular group it is evident that cpx are newly formed, with Al_2O_3
667 and modal content exceeding the PM values. A similar observation is valid for the Porphyroclastic

668 group that, however, do not show an analogous level of enrichment. Cpx from anhydrous
669 harzburgite TRE1 have the highest mg# and the lowest Al_2O_3 content, probably because this sample
670 was less affected by the enrichment process and/or started from the most residual composition.
671 In this framework, the metasomatic process that affected the mantle domain beneath Persani Mts.
672 can be more properly considered as a refertilization that not only modified the composition of the
673 various phases, but also consistently increased the pyroxene modal abundance. Pyroxenes increased
674 at expenses of olivine, as observed by Falus et al. (2008), who described some textures where opx
675 replaces olivine. Spinel was also most probably enriched and/or added to the peridotitic matrix
676 during the refertilization, as testified by its modal abundance, up to 5.3 % in some samples (Table 1
677 ESM), and very high Al_2O_3 content (ESM3-2).
678

679 ## 6.5 Refertilization geodynamic context and subsequent alkaline metasomatism

680 The geochemical affinity of the refertilizing melt can be evaluated thanks to the presence of
681 disseminated amphibole. According to Coltorti et al. (2007b), the geochemical imprint of a
682 metasomatizing agent can be traced back by using key elements (particularly Nb and in general the
683 HFSE, which are highly immobile during chromatoghraphic fractionation processes, Ionov et al.,
684 2002) and their ratios. In Zr/Nb vs Ti/Nb (Fig. 13A) and Zr/Nb vs Ti/Zr (Fig. 13B) diagrams,
685 disseminated amphiboles fall entirely within the "subduction-related" field, a remarkable indication
686 that they were generated by a subduction-related melt, probably a basalt originating from a
687 lithosphere modified by fluids released by the sinking slab. The subducted oceanic plate is still
688 visible today as evidenced by geophysical surveys under the seismically active Vrancea Zone in the
689 southeastern edge of the Carpathian arc (Martin et al., 2006; Edwards & Grasemann 2009; Ismail-
690 Zadeh et al., 2012). Post-collisional magmatism along the East Carpathian range migrated and
691 rejuvenated from NW, where the oldest occurrences are found (10.2 Ma), to SE in the South
692 Harghita volcanic field where the activity is younger than 1 Ma (Mason et al., 1996; Seghedi et al.,
693 2011, 2016 and references therein). The South Harghita calc-alkaline volcanic activity was the last

694 expression of a post-collisional, convergent margin dynamic (Seghedi et al., 2011 and references
695 therein). Asthenospheric upwelling, linked to slab roll-back, was associated with extensional Na
696 and K-alkaline volcanism (Konečný et al., 2002; Seghedi et al., 2011). The calc-alkaline volcanism
697 of the South Harghita developed between 5.3 and 0.3 Ma, with two gaps respectively between 3.9-
698 2.8 and 1.0 Ma (Seghedi et al., 2011; Molnar et al., 2018). During the last gap, the building of Na-
699 alkaline volcanic edifices of Perşani Mts took place (1.2-0.6 Ma), about 40 km to the west (Fig. 1).
700 The last eruptive phase of Perşani Mts occurred contemporaneously with the final stages of South
701 Harghita volcanic activity around 0.6 Ma (Szakács and Seghedi 1995; Pécskay et al., 1995b;
702 Seghedi et al., 2011; Molnar et al., 2018). Although calc-alkaline products do not outcrop in the
703 Perşani Mts, a cognate basaltic block found within the pyroclastic deposits show a clear arc
704 signature (Downes et al., 1995; Mason et al., 1996) and is perfectly comparable to some Călimani-
705 Ghurghiu-Harghita (CGH) basaltic andesites (ESM3-10), supporting the idea that, also in this area,
706 a calc-alkaline magmatic phase (now buried) preceded the alkaline stage.
707 It is thus likely that the mantle under Perşani Mts. indeed largely interacted with calc-alkaline
708 magmas and maybe the majority of melt volumes were trapped and consumed at depth during the
709 refertilization process. The great majority of calc-alkaline magmas of Călimani-Gurghiu-Harghita
710 volcanic chains are differentiated at various degrees and cover different magmatic affinities from
711 low-K andesites to shoshonites (Harangi 2001; Seghedi et al., 2004). The most primitives have
712 Al_2O_3 contents ranging between 16 and 21 wt% and Y as high as 28 ppm (Mason et al., 1996); one
713 of them has Al_2O_3 and MgO around 19.5 and 5 wt%, respectively. This magma is considered as the
714 parental melt of the Călimani series, with $^{87}Sr/^{86}Sr$ and $^{143}Nd/^{144}Nd$ ratios of 0.70525 and 0.51275,
715 respectively, explained by the authors as the result of slight AFC processes that occurred within the
716 crust or, alternatively, of sediment subduction and consequent source contamination. Such a
717 composition fit reasonably well the requirements of the melt responsible for the mantle
718 refertilization recorded in PMVF mantle xenoliths.

719 Disseminated amphiboles clearly have a subduction-related origin while the amphibole vein of
720 lherzolite LAG52 fall in the intraplate field (Fig. 13A, B), showing a striking resemblance with
721 amphibole MXC collected in the pyroclastic deposits of the Perşani Mts (Fig. 14). Continuous
722 variation trends from vein amphiboles to MXC can be observed, with a constant decrease in mg#,
723 Al_2O_3, Na_2O and Cr_2O_3 and an increase in TiO_2 (Fig. 4B) and K_2O. Oxygen and δD isotopic
724 composition of MXC from Perşani and from the Carpathian-Pannonian region support their mantle
725 origin. They are interpreted as fractionation product of basaltic melts (similar to the host alkali
726 basalts, Zanetti et al., 1995) derived by various degrees of partial melting of an asthenospheric
727 source contaminated by fluids released from subducted serpentinites or blueschist like those
728 occurring in the Meliata-Vardar series (Demény et al., 2012 and references therein).
729 Interaction of PMVF mantle with alkaline melts have been already documented and there is good
730 agreement that amphibole vein generation is the main result of this process. Olivine-
731 clinopyroxenites also found as xenoliths in the Perşani Mts volcanics probably represent
732 fractionation products of these alkaline melts formed at depth, within the mantle (Zanetti et al.,
733 1995; Vaselli et al., 1995; Downes et al., 1995; Chalot-Prat & Boullier 1997; Downes, 2001). Being
734 disseminated amphiboles the result from reaction/hydration of cpx, it has to be concluded that the
735 two kinds of amphiboles represent different metasomatic episodes that occurred at different times.
736 Having the interaction with calc-alkaline magmas occurred first, we argue that vein amphibole
737 generation was subsequent to the onset of disseminated amphiboles and may represent the last
738 metasomatic event recorded by PMVF mantle xenoliths. According to Zanetti et al. (1995), some
739 vein amphiboles may represent the "frozen" composition of the alkaline magma travelling through
740 the mantle (Fig. 14). Beside the variable enrichments in LREE, chondrite-normalized REE patterns
741 of LAG52 vein amphiboles are very similar to those found in literature, including amphiboles of
742 clinopyroxenites and MXC. Although the explanation by Zanetti et al. (1995) may be realistic,
743 adcumulates are unlikely to perfectly match a liquid composition (Holness et al., 2017) and vein
744 amphibole are indeed lower in L- and MREE with respect to Perşani Mts lavas. We have thus

745 calculated the melt in equilibrium with LAG52 vein amphibole using $Kd^{amph/alkaline\ melt}$ from GERM
746 database and it resulted almost indistinguishable from the real Perşani alkaline magmas. Calculated
747 cpx in equilibrium with the obtained melt (Fig. 15) is identical to the real cpx from PMVF
748 clinopyroxenites (Vaselli et al., 1995; Chalot-Prat & Boullier, 1997). It has to be underlined that
749 both natural and calculated cpx have completely different compositions, in term of major and trace
750 elements, with respect to those occurring in the refertilized mantle xenoliths. The "magmatic" cpx
751 derived from the alkaline melt/s have different REE patterns (in particular higher LREE and lower
752 HREE, Fig. 15) with respect to the peridotitic ones and could have never been generated by the
753 same liquid. Even using a chromatographic model (Ionov et al., 2002), we could not obtain such
754 HREE enriched diopsides (Yb, 14.4 x Chondrite) starting from the alkaline cpx (Yb, 7.4 x
755 Chondrite) supposing that the alkaline melt was the sole metasomatic agent that acted within PMVF
756 mantle. These considerations further support the hypothesis that cpx and disseminated amphiboles
757 are strictly related and are the result of a previous, calc-alkaline, extremely pervasive refertilization
758 event, distinct from the subsequent alkaline metasomatic episode. The latter, on the other hand,
759 resulted in the generation of amphibole veins within the peridotite and in the crystallization of
760 amphibole-bearing clinopyroxenites and MXC. These magmas, very similar to those erupted by the
761 Persani volcanoes and generated by a new source, crossed the studied lithospheric mantle section in
762 more recent times (most probably after the onset of post-collisional tectonics, Seghedi et al., 2011),
763 at the relatively shallow depth reached in consequence of asthenospheric doming, under a fragile
764 regime. This allowed vein formation with very limited diffusive effects, only detectable as slight
765 LREE and Nb enrichments in some of the pre-existing pyroxenes and their associated amphiboles
766 (Group 2 and 3, Figs. 6 and 8), especially in close proximity of the amphibole vein.
767

768 ## 6.6 Melting and refertilization processes as deduced from noble gas compositions

769 The petrography and mineral chemistry of PMVF ultramafic xenoliths revealed that the extent of
770 melt extraction from local mantle was certainly higher than what can be estimated by the

paragenesis only, mainly composed by pyroxene-rich lherzolites as the result of an extensive re-fertilization of previous depleted mantle matrixes.

In order to further help in deciphering this history, we compared ^{4}He and $^{40}Ar^{*}$ concentrations and $^{4}He/^{40}Ar^{*}$ in FI with the mg#. In a recent study from Lower Silesia, Rizzo et al. (2018) showed that the chemistry of FI and minerals coupled to $^{4}He/^{40}Ar^{*}$ ratio may provide insights of the extent of partial melting, as well as on the occurrence of metasomatic processes that masked the pristine SCLM characteristics. This is related to the different crystal–melt partitioning of ^{4}He and $^{40}Ar^{*}$ for olivine and cpx (Heber et al., 2007).

Olivine of PMVF xenoliths represent the most likely candidate for identifying the residual mantle, bearing in mind that increasing mg# should indicate higher extent of partial melting, leading to a depleted lithology (Herzberg et al., 2016; Rizzo et al., 2018). In the few samples not affected by diffusive fractionation (LAG52, BARQ4, TRE2), a progressive decrease of ^{4}He and $^{40}Ar^{*}$ concentrations at increasing mg# (from 89.2 to 90.7) can be noticed (ESM3-11), which is compatible with a partial melting effect. This is supported by the $^{4}He/^{40}Ar^{*}$ ratio that decreases from 2.2 to 1.4 at increasing mg#, being $^{4}He/^{40}Ar^{*}$ within the reported range for mantle production. These evidences indicate that the extent of partial melting was low. Indeed, as for comparison, olivine from Lower Silesia mantle having a $^{4}He/^{40}Ar^{*}$ ~0.3 record a residual mantle that was strongly depleted (25–30% of partial melting, Rizzo et al., 2018). Alternatively, we may suppose that olivine recrystallized during or after a metasomatic/refertilization process by trapping FI with $^{4}He/^{40}Ar^{*}$ typical of mantle production. If so, we would not have any more trace of primary FI resembling the residual mantle features. However, the very small number of reliable olivine data (i.e., not affected by diffusive fractionation) does not give robustness to these inferences.

Looking at opx and cpx, most of the samples do not show any relation between ^{4}He, $^{40}Ar^{*}$ concentrations, $^{4}He/^{40}Ar^{*}$ ratios and Mg# (ESM3-11). The only exception is for LAG52 that has the highest ^{4}He and $^{40}Ar^{*}$ concentrations at the lowest mg#, compatible with low extent of partial melting relatively to the other samples; however, in terms of $^{4}He/^{40}Ar^{*}$ this sample has not the

highest values (ESM3-11), as expected in case of partial melting as main process. This means that LAG52 did not maintain any memory of the partial melting history. In terms of $^{4}He/^{40}Ar^{*}$, opx and cpx present a $He/^{40}Ar^{*}$ in the range 0.2-1.2, without any particular trend. Apart sample TRE3, opx and cpx have $^{4}He/^{40}Ar^{*}>0.6$. These values are not compatible with the degrees of melting estimated by using mineral chemistry (see Section 6.4). This behaviour suggests that most of opx and cpx recrystallized, as consequence of the refertilization process, by trapping a new population of FI with a distinct composition that masked the partial melting history. Interestingly, opx and cpx of samples TRE1, TRE2, and TRE4 plot out of the above range of values, showing mg# > 90.9 and $^{4}He/^{40}Ar^{*}$ between 1.3 and 2.5. In detail, these samples show a gradual increase of mg# and $^{4}He/^{40}Ar^{*}$ that cannot be explained with either partial melting or with refertilization process, due to their strong depletion. The most reasonable explanation for the FI chemistry of these samples involves the entrapment of secondary FI from the latest alkaline metasomatism or from the host magma that resemble more "magmatic-like" $^{4}He/^{40}Ar^{*}$ values. This interpretation is further supported by the $^{3}He/^{4}He$ values (6.5-6.8 Ra), which are the highest of the entire dataset and clearly higher than the other opx (5.4-6.4 Ra) and cpx (5.3-6.1) as well as of olivine (5.2-5.9 Ra) (ESM3-11). It is worth noting that two of these samples belong to the low-temperature, high-stress *Po. s.s.* textural sub-group (Table 1), probably more prone to fluid percolation. We argue that the $^{3}He/^{4}He$ signature of fluids trapped in opx and cpx of samples TRE1, TRE2, and TRE4 can be related to MORB-like asthenospheric fluids that penetrated the local mantle and partially mixed with residual fluids contaminated by the recycling of crustal (subduction-related) material.

Resuming, the comparison of FI and mineral chemistry mostly points toward a local mantle originally depleted by rather high extents of partial melting and then re-fertilized by subduction-related fluids. A small portion of the mantle also bears memory of the latest alkaline metasomatism or the infiltrated host magma.

6.7 Subduction of crustal material and the origin of alkaline magmatism

In order to make inferences on the noble gas signature of SCLM beneath PMVF, we now focus on the He and Ne isotope compositions and compare them with other European localities.

The range of $^{3}He/^{4}He$ measured in olivine (only three reliable measures from LAG52, BARQ4, and TRE2), opx, and cpx (excluding sample TRE1, TRE2, and TRE4) is 5.8±0.2 Ra (Figs. 10 and 12 and ESM3-11). This range is comparable to the few $^{3}He/^{4}He$ measurements existing for xenoliths from PMVF and analysed with a crushing technique, which yielded 5.6 and 6.0 Ra (Althaus et al., 1998; Kis et al., 2019). However, the authors do not provide details on what mineral phase they analysed as well as Althaus et al. (1998) do not explicit the type of crushing (single- or multi-step). This suggests that the mantle beneath PMVF is more radiogenic than the typical MORB range (8±1 Ra; Graham, 2002). Previous studies carried out in other mantle xenoliths from western and central European volcanic provinces (i.e., Eifel, French Massif Central, Pannonian Basin, Calatrava, Tallante, and Lower Silesia) yielded a whole $^{3}He/^{4}He$ range of 6.3±0.4 Ra (Gautheron et al., 2005; Martelli et al., 2011; Rizzo et al., 2018). Therefore, we could conclude that the mantle beneath PMVF is within European SCLM range. However, if we compare the range of values measured in each of the European locations, some differences can be underlined (Figs. 10 and 12). Mantle xenoliths from Eifel, French Massif Central, Pannonian Basin, Calatrava, and Lower Silesia in fact show $^{3}He/^{4}He$ of 6.5±0.3 Ra, 6.4±0.2 Ra, 6.5±0.1 Ra, 6.3±0.1 Ra, and 6.2±0.3 Ra, respectively, while those from Tallante and PMVF have 5.6±0.1 Ra and 5.8±0.2 Ra, respectively. For sake of clarity, we point out that data from Eifel, French Massif Central, and Pannonian Basin only regard olivine (Gautheron et al., 2005), while those from Calatrava olivine and opx (Martelli et al., 2011), and those from Lower Silesia olivine, opx, and cpx (Rizzo et al., 2018) like in this study. PMVF and Tallante show the lowest range of $^{3}He/^{4}He$, while the other European locations are comparable and have slightly but significantly higher ratios.

Gautheron et al. (2005) justified the average $^{3}He/^{4}He$ signature of the European SCLM, proposing two interpretative scenarios: i) a recent and local metasomatism by a MORB-like He composition rising from the asthenosphere and mixing with a more-radiogenic isotope signature produced in the

849 lithosphere or ii) a global SCLM steady state in which a flux of ^{3}He-rich fluids originated from the
850 asthenosphere mixes with ^{4}He-rich fluids/melts recycled in the lithosphere from U-Th decay of
851 crustal material. This material could derive from dehydration of active or fossil subducting slabs
852 (e.g., Yamamoto et al., 2004; Faccenna et al., 2010).
853 Therefore, the ^{3}He/^{4}He signature of mantle beneath PMVF can be interpreted with the models
854 proposed by Gautheron et al. (2005), assuming an enhanced recycling of crustal material in the
855 local lithosphere respect to other European portions. This crustal material addition can be justified
856 considering the recent subduction that occurred in eastern Carpathians (Seghedi et al., 2011 and
857 references therein), similarly to what has been inferred for Tallante (Martelli et al., 2011 and
858 references therein).
859 The low noble gases (and CO_2) concentration, as well as the ^{3}He/^{4}He in PMVF mantle xenoliths
860 with respect to other parts of the European SCLM (Gautheron et al., 2005; Rizzo et al., 2018),
861 support a subduction-related imprint of fluids circulating in the local mantle at the time of re-
862 fertilization.
863 The apparent paradox between a fluid-rich environment, such as the subduction setting, and the low
864 concentration of noble gases, could be reconciled inferring that these fluids were reasonably richer
865 in H_2O than in CO_2. Because CO_2 is the main carrier of noble gases at whatever depth of circulation
866 (i.e., mantle or crust; Anderson, 1998), this could explain the low ^{4}He and ^{40}Ar* concentrations in
867 FI from PMVF. The diffusive fractionation of noble gas observed in these mantle portions could
868 also evidence a continue mantle recrystallization due to the stresses related to asthenospheric
869 upwelling.
870 Ne isotope ratios give indications similar to the ^{3}He/^{4}He ratio. Indeed, Fig. 9 shows that PMVF
871 ^{21}Ne/^{22}Ne and ^{20}Ne/^{22}Ne plot along or slightly below the theoretical mixing line between air and a
872 MORB-like mantle. Data slightly below this mixing line can be interpreted as a three component
873 mixing that includes crustal material (see caption for further details on crustal end-member)
874 (Kennedy et al., 1990; Ballentine, 1997; Ballentine et al., 2005). This supports the idea based on

875 $^{3}He/^{4}He$ ratio that mantle beneath PMVF was metasomatized/refertilized by subduction-related
876 fluids that was responsible for recycling of crustal material in the local SCLM. Mason et al. (1996)
877 indeed invoked a fluid modified depleted mantle as the source of South Harghita calc-alkaline
878 magmas. According to the authors, such a source may have been contaminated by the subduction of
879 a small amount of Oligocene flysch material from the Carpathians accretionary wedge; however,
880 the main crustal component was not identified.
881 Finally, the evidences from He and Ne isotope compositions exclude the presence of a plume below
882 PMVF. In fact, the plume-related signature should have $^{3}He/^{4}He$ values above the MORB range (>9
883 Ra) and a lower $^{21}Ne/^{22}Ne$ ratio for a given $^{20}Ne/^{22}Ne$ than MORB melts (Kurz et al., 2009;
884 Moreira, 2013 and references therein) (Figs. 10 and 9). As stated above, the ranges of He and Ne
885 isotope ratios are comparable to those for other European regions where no plume is present
886 (Gautheron et al., 2005; Moreira et al., 2018).
887
888 ## 6.8 Comparison with gases emitted in the Eastern Carpathians
889 In the south-eastern Carpathian-Pannonian Region either anorogenic or orogenic magmas erupted
890 since 11 Ma (Szakács et al., 1993; Seghedi et al., 2004, 2011). Although volcanic activity in the
891 PMVF seems now extinct, the presence of strong CO_2 degassing in the neighbouring Ciomadul
892 volcanic area (about 40 km to the east) may indicate that magmatism is still active at depth
893 (Oncescu et al., 1984; Althaus et al., 2000; Vaselli et al., 2002; Popa et al., 2012; Kis et al., 2017,
894 2019 and references therein). Indeed, many gas emissions are present (Althaus et al., 2000; Vaselli
895 et al., 2002 Kis et al., 2017, 2019 and references therein), emitting in the atmosphere a huge amount
896 of CO_2 (8.7×10^{3} t/y) comparable to other >10 kyr dormant volcanoes worldwide (Kis et al., 2017).
897 These evidences pose a hazard of CO_2 outpourings for local inhabitants and visitors (Kis et al.,
898 2017, 2019).
899 These gas manifestations are the closest to the mantle xenoliths outcropping area for comparing the
900 noble gas composition. The $^{3}He/^{4}He$ values from Stinky Cave (Puturosul), Dobogeni, and

Balvanyos are up to 3.2, 4.4, and 4.5 Ra, respectively, indicating the presence of a magma not yet completely cooled down (Althaus et al., 2000; Vaselli et al., 2002). In the Ciomadul area, Kis et al. (2019) measured $^{3}He/^{4}He$ up to 3.1 Ra, arguing that these values are indicative of a mantle lithosphere strongly contaminated by subduction-related fluids and post-metasomatic ingrowth of radiogenic ^{4}He. This hypothesis differs from what proposed by Althaus et al. (2000) and Vaselli et al. (2002) and presumes a small scale (~40 km) spatial heterogeneity in the local mantle of ~3 unit Ra, considering that the range of $^{3}He/^{4}He$ measured in mantle xenoliths from PMVF is up to 6.8 Ra (Kis et al., 2019 and this study).

The hypothesis by Kis et al. (2019) is in some circumstances in contradiction with their same considerations, as well as with previous studies. Kis et al. (2019) indicate that 3% of crustal assimilation could be sufficient to lower the $^{3}He/^{4}He$ of a hypothetical local mantle (5.95 Ra, as they measured in cpx from a PMVF xenolith) to their measured values (3.1 Ra), in accordance with the petrological evidences in calc-alkaline rocks provided by Mason et al. (1996). Kis et al. (2019) however, favor the hypothesis that 3.1 Ra is representative of the local mantle signature. In their magma ageing calculation, starting from the U and Th content in a selected dacite, the Authors suggest that after 30 Kyr (last eruption at Ciomadul) the $^{3}He/^{4}He$ ratio of 5.95 Ra could be lowered at 4.65 Ra. Because this value is higher than 3.1 Ra measured in their study, Kis et al. (2019) consider unlikely this process. We point out that Vaselli et al. (2002) measured up to 4.4 and 4.5 Ra in Doboşeni and Balvanyos gases, respectively, being these values comparable to their calculation outcome. However, Kis et al. (2019) ignore Vaselli et al. (2002) values that instead support the reliability of magma ageing process in explaining the isotopic signature of gas emissions. In the conclusions, Kis et al. (2019) state that the mantle below Ciomadul has a low $^{3}He/^{4}He$ signature but also argue that variable degrees of interaction with crustal gases may occur, although some of them can survive this interaction maintaining their primary signature.

For the above reasons, we consider more likely that magmatic gases from Ciomadul volcano are not representative of local mantle but are released from a cooling and aging magma that resides within

927 the crust or are contaminated by crustal fluids during their upraise to the surface, as already
928 proposed by Althaus et al. (2000) and Vaselli et al. (2002).
929
930 ## 7. CONCLUSIONS
931 The lithospheric mantle beneath the Eastern Transylvanian Basin was investigated through a suite
932 of ultramafic xenoliths mainly composed of lherzolites with minor harzburgites and olivine-
933 clinopyroxenites. The formers are extremely fertile (cpx content up to 22%) and characterized by
934 the almost ubiquitous presence of disseminated amphibole and a continuous textural variation from
935 recrystallized protogranular to porphyroclastic types.
936 Petrographic features, whole rock and mineral chemistry and noble gases (He, Ne, Ar) systematics
937 in FI reveal a complex evolution of this mantle section. Porphyroclastic samples still bear clues of
938 variable degrees of partial melting, as testified by high mineral mg# and depleted opx M-HREE
939 patterns. On the other hand, the high cpx modal contents and the Al_2O_3 contents and REE patterns
940 of the pyroxenes in the protogranular samples are not compatible with simple melting processes, but
941 can be explained by a pervasive refertilization event that erased, in most of the cases, the evidence
942 of the pristine depleted parageneses. The high Al_2O_3 contents of pyroxenes and spinel and the
943 HFSE ratios of disseminated amphiboles point toward a calc-alkaline nature for the refertilizing
944 magma that was similar to the most primitive basalts of the Călimani series. A further support to
945 this hypothesis derive from the finding, within PMVF pyroclastic sequences, of a lithic cognate of
946 calc-alkaline affinity 1Ma older that the alkali basalts comparable to some basaltic andesites of the
947 CGH chain (Downes et al., 1995). The studied mantle section also shows evidences of interaction
948 with melts of different kind, visible from slight LREE enrichments in pyroxenes and amphibole
949 vein formation. This metasomatic event is linked to the passage of alkaline melts similar to the host
950 lavas, as testified by the close resemblance between the amphibole vein and the megacrystals also
951 found in the Perşani Mts pyroclastic deposits.

952 In PMVF xenoliths, FI are mostly secondary. The isotope compositions of Ne and Ar and,
953 complementarily, the $^{4}He/^{20}Ne$ ratio highlights a variable air contamination, progressively
954 decreasing from olivine to cpx. This contamination seems a local mantle feature inherited from the
955 recycling of subduction-related fluids, occurred during last orogenic event in Eastern Carpathians.
956 Diffusive fractionation likely modified the noble gases composition of the residual mantle during its
957 melting, but this process can be appreciated only in olivine with ^{4}He and $^{40}Ar^{*}$ concentrations
958 below ~$1.0\text{-}2.0\times10^{-13}$ mol/g. The comparison of ^{4}He and $^{40}Ar^{*}$ concentrations as well as $^{4}He/^{40}Ar^{*}$
959 with the mg# of olivine, opx, and cpx does not show clear variations due to partial melting, thus, we
960 infer that most of the pyroxenes recrystallized, as consequence of the refertilization process by
961 subduction-related melts. A small portion of the mantle also bears memory of the latest alkaline
962 metasomatism or the host magma, as testified by $^{4}He/^{40}Ar^{*}$ and $^{3}He/^{4}He$ values in those samples
963 more texturally prone to fluid infiltration. Excluding these latter, the range of $^{3}He/^{4}He$ measured in
964 olivine, opx, and cpx is 5.8±0.2 Ra, which is more radiogenic than the typical MORB mantle (8±1
965 Ra) and among the lowest values proposed for western and central European volcanic provinces
966 (6.3±0.4 Ra). We argue that the $^{3}He/^{4}He$ signature of mantle beneath PMVF reflects an enhanced
967 recycling of crustal material in the local lithosphere with respect to other European portions. Ne
968 isotope ratios give indications similar to the $^{3}He/^{4}He$ ratio, with $^{21}Ne/^{22}Ne$ and $^{20}Ne/^{22}Ne$ data
969 plotting along, or slightly below, the theoretical mixing line between air and a MORB-like mantle.
970 Data slightly below this mixing line can be interpreted as a three component mixing that includes
971 crustal material. This supports the idea based on $^{3}He/^{4}He$ ratio that mantle beneath PMVF was
972 metasomatized/refertilized by subduction-related fluids responsible for the recycling of crustal
973 material in the local SCLM.
974 The evidences from He and Ne isotope compositions exclude the presence of a plume below
975 PMVF.
976 Comparing the xenolith $^{3}He/^{4}He$ signature with that of CO_2-dominated gas emissions located
977 around Ciomadul volcanic complex (up to 4.5 Ra), located only about 40 km to the east of our study

978 area, we conclude that surface gases are not representative of the local mantle. Rather, they are
979 released from a cooling and aging magma residing within the crust or, alternatively, they are
980 contaminated by crustal fluids during their rising toward the surface.
981
982 ## ACKNOWLEDGMENTS
983 The noble gas contribution in this work is part of the PhD (XXXII cycle) of Andrea Luca Rizzo at
984 the University of Ferrara. We thank Mariagrazia Misseri for helping in samples preparation and
985 isotope analysis of noble gases from fluid inclusions. We are grateful to Mariano Tantillo for his
986 support in noble gas laboratory activities. I.S. was supported by grant of Ministry of Research and
987 Innovation, CNCS – UEFISCDI, project number PN-III-P4-ID-PCCF-2016-4-0014, within PNCDI
988 III.
989
990 ## 8. REFERENCES
991 Abe, N., Arai, S., Yurimoto, H., 1998. Geochemical characteristics of the uppermost mantle
992 beneath the Japan island arcs; implications for upper mantle evolution. Physics of the
993 Earth and Planetary Interiors 107, 233–48.

994 Althaus, T., Niedermann, S., Erzinger, J., 1998. Noble gases in ultramafic mantle xenoliths
995 of the Persani Mountains, Transylvaninan Basin, Romania. Goldschmidt Conference
996 Toulouse 1998 Abstract book, Mineralogical Magazine 62A.

997 Althaus, T., Niedermann, S., Erzinger, J., 2000. Noble gas studies of fluids and gas
998 exhalations in the East Carpathians, Romania. Chemie der Erde 60, 189–207.

999 Anderson, D.L., 1998. A model to explain the various paradoxes associated with mantle
1000 noble gas geochemistry. Proceedings of the National Academy of Sciences USA 95,
1001 9087-9092.

1002 Arai, S., Ishimaru, S., Okrugin, V.M., 2003. Metasomatized harzburgite xenoliths from
1003 Avacha volcano as fragments of mantle wedge of the Kamchatka arc: Implication for
1004 the metasomatic agent. The Island Arc 12, 233-246.

1005 Arai, S., Takada, S., Michibayashi, K., Kida, M., 2004. Petrology of peridotite xenoliths
1006 from Iraya Volcano, Philippines, and its implication for dynamic mantle-wedge
1007 processes. Journal of Petrology 45, 369-389.

1008 Arai, S., Ishimaru, S., 2008. Insights into petrological characteristics of the lithosphere of
1009 mantle wedge beneath arcs through peridotite xenoliths: a review. Journal of Petrology
1010 49, 665–695.

1011 Bali, E., Szabó, C., Vaselli, O., Török, K., 2002. Significance of silicate melt pockets in
1012 upper mantle xenoliths from the Bakony–Balaton Highland Volcanic Field, Western
1013 Hungary. Lithos 61, 79– 102.

1014 Ballentine, C.J., 1997. Resolving the mantle He/Ne and crustal $^{21}Ne/^{22}Ne$ in well gases.
1015 Earth and Planetary Science Letters 152, 233–249.

1016 Ballentine, C.J., Marty, B., Sherwood Lollar, B., Cassidy, M., 2005. Neon isotopes constrain
1017 convection and volatile origin in the Earth's mantle. Nature 433, 33–38.

1018 Ballhaus, C., Berry, R.F., Green, D.H., 1991. High pressure experimental calibration of the
1019 olivine-orthopyroxene-spinel oxygen barometer: implications for the oxidation state of
1020 the mantle. Contribution to Mineralogy and Petrology 107, 27-40.

1021 Bénard, A., Woodland, A.B., Arculus, R.J., Nebel, O., McAlpine, S.R.B., 2018. Variation in
1022 sub-arc mantle oxygen fugacity during partial melting recorded in refractory peridotite
1023 xenoliths from the West Bismarck Arc. Chemical Geology 486, 16-30.

1024 Bernstein, S., Kelemen, P.B., Hanghøj, K., 2007. Consistent olivine Mg# in cratonic mantle
1025 refl ects Archean mantle melting to the exhaustion of orthopyroxene. Geology 35, 459-
1026 462.

1027 Bianchini, G., Beccaluva, L., Nowell, G.M., Pearson, D.G., Siena, F., 2011. Mantle
1028 xenoliths from Tallante (Betic Cordillera): Insights into the multi-stage evolution of
1029 the south Iberian lithosphere. Lithos 124, 308-318.

1030 Bonadiman, C., Beccaluva, L., Coltorti, M., Siena, F., 2005. Kimberlite-like metasomatism
1031 and 'garnet signature' in spinelperidotite xenoliths from Sal, Cape Verde Archipelago:
1032 relics of a subcontinental mantle domain within the Atlantic Oceanic lithosphere?
1033 Journal of Petrology 46, 2465-2493.

1034 Bonadiman, C., Coltorti, M., 2011. Numerical modelling for peridotite phase melting trends
1035 in the SiO_2-Al_2O_3-FeO-MgO-CaO system at 2 GPa. 21° Goldschmidt Conf., August
1036 14-19, 2011, Prague. Mineralogical Magazine, 75(3), 548.

1037 Bonadiman, C., Nazzareni, S., Coltorti, M., Comodi, P., Giuli, G., Faccini, B., 2014. Crystal
1038 chemistry of amphiboles: implications for oxygen fugacity and water activity in
1039 lithospheric mantle beneath Victoria Land, Antarctica. Contribution to Mineralogy and
1040 Petrology 167: 984, DOI 10.1007/s00410-014-0984-8.

1041 Bonadiman, C., Coltorti, M., 2018. Mantle subsolidus and melting behavior as modelled in
1042 the system CMASFe. 3rd European Mantle Workshop, Pavia, June 26-28, 2018,
1043 Abstract Book.

1044 Bonatti, E., Peyve, A., Kepezhinskas, P., Kurentsova, N., Seyler, M., Skolotnev, S.,
1045 Udintsev, G., 1992. Upper mantle heterogeneity below the Mid-Atlantic Ridge, 0–
1046 15N. Journal of Geophysical Research 97, 4461–4476.

1047 Bonatti, E., Seyler, M., Sushevskaya, N., 1993. A cold suboceanic mantle belt at the Earth's
1048 equator. Science 261, 315–320.

1049 Brandon, A.D., Draper, D.S., 1996. Constraints on the origin of the oxidation state of mantle
1050 overlying subduction zones: an example from Simcoe, Washington, USA. Geochimica
1051 et Cosmochimica Acta 60, 1739–1749.

1052 Brey, G.P., Köhler, T., 1990. Geothermobarometry in the four-phase lherzolites II. New
1053 Thermobarometers and practical assessment of existing thermobarometers. Journal of
1054 Petrology 31, 1353-1378.

1055 Bryant, J.A., Yogodzinsky, G.M., Churikova, T.G., 2007. Melt-mantle interactions beneath
1056 the Kamchatka arc: evidence from ultramafic xenoliths from Shiveluch volcano.
1057 Geochemistry Geophysics Geosystems 8, Q04007, doi:10.1029/2006GC001443,
1058 ISSN: 1525-2027.

1059 Burnard, P., Graham, D., Turner, G., 1997. Vesicle-specific noble gas analyses of "popping
1060 rock": Implications for primordial noble gases in earth. Science 276, 568–571.

1061 Burnard, P.G., Farley, K., Turner, G., 1998. Multiple fluid pulses in a Samoan harzburgite.
1062 Chemical Geology 147, 99–114.

Burnard, P., 2004. Diffusive fractionation of noble gases and helium isotopes during mantle melting. Earth and Planetary Science Letters 220, 287–295.

Chalot-Prat, F., Bouillier, A-M., 1997. Metasomatism in the subcontinental mantle beneath the Eastern Carpathians (Romania): new evidence from trace element geochemistry. Contribution to Mineralogy and Petrology 129, 284-307.

Coltorti, M., Bonadiman, C., Faccini, B., Ntaflos, T., Siena, F., 2007a. Slab melt and intraplate metasomatism in Kapfenstein mantle xenoliths (Styrian Basin, Austria). Lithos 94, 66-89.

Coltorti, M., Bonadiman, C., Faccini, B., Grégoire, M., O'Reilly, S.Y., Powell, W., 2007b. Amphiboles from suprasubduction and intraplate lithospheric mantle. Lithos 99, 68-84.

Créon, L., Rouchon, V., Youssef, S., Rosenberg, E., Delpech, G., Szabó, C., Remusat, L., Mostefaoui, S., Asimow, P. D., Antoshechkina, P. M., et al., 2017. Highly CO_2-supersaturated melts in the Pannonian lithospheric mantle – A transient carbon reservoir? Lithos 286–287, 519–533.

Demény, A., Vennemann, T.W., Homonnay, Z., Milton, A., Embey-Isztin, A., Nagy, G., 2005. Origin of amphibole megacrysts in the Pliocene-Pleistocene basalts of the Carpathian-Pannonian region. Geologica Carpathica 56, 179-189.

Demény, A., Harangi, S., Vennemann, T.W., Casillas, R., Horvát, P., Milton, A.J., Mason, P.R.D., Ulianov, A., 2012. Amphiboles as indicators of mantle source contamination: Combined evaluation of stable H and O isotope compositions and trace element ratios. Lithos 152, 141-156.

Dick, H.J.B., Natland, J.H., 1996. Late stage melt evolution and transport in the shallow mantle beneath the East Pacific Rise, in: Gillis, K., Mevel, C. and Allan, J. (Eds), Proceedings of the Ocean Drilling Program, Scientific Results, v. 147, Texas A&M University, Ocean Drilling Program, College Station, TX.

Downes, H., Seghedi, I., Szakács, A., Dobosi, G., James, D.E., Vaselli, O., Rigby, I.J., Ingram, G.A., Rex, D., Pécskay, Z., 1995. Petrology and geochemistry of the late Tertiary/Quaternary mafic alkaline volcanism in Romania. Lithos 35, 65–81.

1092 Downes, H., 2001. Formation and modification of the shallow sub-continental lithospheric
1093 mantle: a review of geochemical evidence from ultramafic xenolith suites and
1094 tectonically emplaced ultramafic massifs of Western and Central Europe. Journal of
1095 Petrology 42, 233-250.

1096 Edwards, M.A., Grasemann, B., 2009. Mediterranean snapshots of accelerated slab retreat:
1097 subduction instability in stalled continental collision. Geological Society, London,
1098 Special Publication 311, 155-192.

1099 Embey-Isztin, A., Dobosi, G., Altherr, R., Meyer, H.-P., 2001. Thermal evolution of the
1100 lithosphere beneath the western Pannonian Basin: evidence from deep seated
1101 xenoliths. Tectonophysics 331, 285-306.

1102 Faccenna, C., Becker, T.W., Lallemand, S., Lagabrielle, Y., Funiciello, F., Piromallo, C.,
1103 2010. Subduction-triggered magmatic pulses: a new class of plumes? Earth and
1104 Planetary Science Letters 299, 54–68.

1105 Faccini, B., Bonadiman, C., Coltorti, M., Grégoire, M., Siena, F., 2013. Oceanic material
1106 recycled within the sub-Patagonian lithospheric mantle (Cerro del Fraile, Argentina).
1107 Journal of Petrology 54, 1211-1258.

1108 Falus, G., Szabó, C., Vaselli, O., 2000. Mantle upwelling within the Pannonian Basin:
1109 evidence from xenolith lithology and mineral chemistry. Terra Nova 12, 295-302.

1110 Falus, G., Tommasi, A., Ingrin, J., Szabó, C., 2008. Deformation and seismic anisotropy of
1111 the lithospheric mantle in the southeastern Carpathians inferred from the study of
1112 mantle xenoliths. Earth and Planetary Science Letters 272, 50–64.

1113 Falus, G., Tommasi, A., Soustelle, V., 2011. The effect of dynamic recrystallization on
1114 olivine crystal preferred orientations in mantle xenoliths deformed under varied stress
1115 conditions. Journal of Structural Geology 33, 1528-1540.

1116 Foley, S.F., 2011. A reappraisal of redox melting in the Earth's Mantle as a function of
1117 tectonic setting and time. Journal of Petrology 52, 1363-1391.

1118 Forshaw, J.B., Waters, D.J., Pattison, D.R.M., Palin, R.M., Gopon, P., 2019. A comparison
1119 of observed and thermodynamically predicted phase equilibria and mineral
1120 compositions in mafic granulites. Journal of Metamorphic Geology 37, 153-179.

1121 Franz, L., Becker, K.P., Kramer, W., Herzig, P.M., 2002. Metasomatic mantle xenoliths
1122 from the Bismarck microplate (Papua New Guinea) – Thermal evolution,
1123 geochemistry and extent of slab-induced metasomatism. Journal of Petrology 43, 315-
1124 343.

1125 Gautheron, C., Moreira, M., Allègre, C., 2005. He, Ne and Ar composition of the European
1126 lithospheric mantle. Chemical Geology 217, 97–112.

1127 Gîrbacea, R., Frisch, W., Linzer, H.-G., 1998. Post-orogenic uplift induced extension: a
1128 kinematic model for the Pliocene to recent tectonic evolution of the Eastern
1129 Carpathians (Romania). Geologica Carpathica 49, 315–327.

1130 Graham, 2002. Noble gas isotope geochemistry of Mid-Ocean Ridge and Ocean Island
1131 Basalts: characterization of mantle source reservoirs. Review of Mineralogy and
1132 Geochemistry 47, 247–317.

1133 Grégoire, M., McInnes, B.I.A., O'Reilly, S.Y., 2001. Hydrous metasomatism of oceanic sub-
1134 arc mantle, Lihir, Papua New Guinea — part 2. Trace element characteristics of slab-
1135 derived fluids. Lithos 59, 91–108.

1136 Harangi, S., 2001. Neogene to Quarternary volcanism of the Carpathian-Pannonian Region
1137 – a review. Acta Geologica Hungarica 44, 223-258.

1138 Harangi, S., Sági, T., Seghedi, I., Ntaflos, T., 2013. A combined whole-rock and mineral-
1139 scale investigation to reveal the origin of the basaltic magmas of the Perşani
1140 monogenetic volcanic field, Romania, eastern-central Europe. Lithos 180–181, 43-57.

1141 Harangi, S., Jankovics, M. É., Sági, T., Kiss B., Lukács R., Soós I., 2014. Origin and
1142 geodynamic relationships of the Late Miocene to Quaternary alkaline basalt volcanism
1143 in the Pannonian basin, eastern–central Europe. International Journal of Earth Sciences
1144 (Geol Rundsch) 104, 2007-2032.

1145 Hawthorne, F.C., Oberti, R., 2007. Amphiboles: crystal chemistry. Reviews in Mineralogy
1146 and Geochemistry 67, 1–54.

1147 Heber, V.S., Brooker, R.A., Kelley, S.P., Wood, B.J., 2007. Crystal-melt partitioning of
1148 noble gases (helium, neon, argon, krypton, and xenon) for olivine and clinopyroxene.
1149 Geochimica et Cosmochimica Acta 71, 1041–1061.

1150 Heber, V.S., Wieler, R., Baur, H., Olinger, C., Friedmann, A., Burnett, D.S., 2009. Noble
1151 gas composition of the solar wind as collected by the Genesis mission. Geochimica et
1152 Cosmochimica Acta 73, 7414–7432.

1153 Hellebrand, E., Snow, J.E., Dick, H.J.B., Hofmann, A.W., 2001. Coupled major and trace
1154 elements as indicators of the extent of melting in mid-ocean-ridge peridotites. Nature
1155 410, 677-681.

1156 Herzberg, C., Vidito, C., Starkey, N.A., 2016. Nickel–cobalt contents of olivine record
1157 origins of mantle peridotite and related rocks. American Mineralogist 101,1952–1966.

1158 Hilton, D.R., Hammerschmidt, K., Teufel, S., Friedrichsen, H., 1993. Helium isotope
1159 characteristics of Andean geothermal fluids and lavas. Earth and Planetary Science
1160 Letters 120, 265–282.

1161 Hilton, D.R., Fischer, T.P., Marty, B., 2002. Noble Gases and Volatile Recycling at
1162 Subduction Zones. Reviews in Mineralogy and Geochemistry 47, 319–370.

1163 Holness, M.B., Vukmanovic, Z., Mariani, E., 2017. Assessing the role of compaction in the
1164 formation of adcumulates: a microstructural perspective. Journal of Petrology 58, 643-
1165 674.

1166 Ismail-Zadeh, A., Matenco, L., Radulian, M., Cloetingh, S., Panza, G., 2012. Geodynamics
1167 and intermediate-depth seismicity in Vrancea (the south-eastern Carpathians): current
1168 state-of-the art. Tectonophysics 530–531, 50–79.

1169 Jamieson, H.E., Roeder, P.L., 1984. The distribution of Mg and Fe^{2+} between olivine and
1170 spinel at 1300°C. American Mineralogist 69, 283-291.

1171 Johnson, K.T.M., Dick, H.J.B., Shimizu, N., 1990. Melting in the oceanic upper mantle: an
1172 Ion Microprobe study of diopsides in abyssal peridotites. Journal of Geophysical
1173 Research 95, 2661-2678.

1174 Kennedy, B.M., Hiyagon, H., and Reynolds, J.H., 1990. Crustal neon: a striking uniformity.
1175 Earth and Planetary Science Letters 98, 277-286.

1176 Kepezhinskas, P., Defant, M.J., Drummond, M.S., 1996. Progressive enrichment of island
1177 arc mantle by metl-peridotite interaction inferred from Kamchatka xenoliths.
1178 Geochimica et Cosmochimica Acta, 60, 1217-1229.

Kis, B.M., Ionescu, A., Cardellini, A., Harangi, S., Baciu, C., Caracausi, A., Viveiros, F. 2017. Quantification of carbon dioxide emissions of Ciomadul, the youngest volcano of the Carpathian-Pannonian Region (Eastern-Central Europe, Romania). Journal of Volcanology and Geothermal Research 341, 119–130.

Kis, B.M., Caracausi, Palcsu, L., Baciu, C., A., Ionescu, A., Futó, I., Sciarra, A., Harangi, S. 2019. Noble gas and carbon isotope systematics at the seemingly inactive Ciomadul volcano (Eastern-Central Europe, Romania): evidence for volcanic degassing. Geochemistry, Geophysics, Geosystems, https://doi.org/10.1029/2018GC008153.

Klemme, S., 2007. The influence of Cr on the garnet–spinel transition in the Earth's mantle: experiments in the system $MgO–Cr_2O_3–SiO_2$ and thermodynamic modeling. Lithos 77, 639-646.

Koněcný, V., Kováč, M., Lexa, J., Šefara, J., 2002. Neogene evolution of the Carpatho-Pannonian region: an interplay of subduction and back-arc diapiric uprise in the mantle. EGU Stephan Mueller Special Publication Series 1, 105-123.

Kovács, I., Patkó, L., Falus, G., Aradi, L.E., Szanyi, G., Gráczer, Z., Szabó, C., 2018. Upper mantle xenoliths as sources of geophysical information: the Perşani Mts. area as a case study. Acta Geodaetica et Geophysica, https://doi.org/10.1007/s40328-018-0231-2.

Kurz, M.D., Curtice, J., Fornari, D., Geist, D., Moreira, M., 2009. Primitive neon from the center of the Galápagos hotspot. Earth and Planetary Science Letters 286, 23–34.

Kurz, M.K., 1986. Cosmogenic helium in a terrestrial igneous rock. Nature 320, 435–439.

Ionov, D.A., Hofmann, A.W., 1995. Nb-Ta-rich mantle amphiboles and micas: implications for subduction-related metasomatic trace element fractionations. Earth and Planetary Science Letters 131, 341-356.

Ionov, D.A., Griffin, W.L., O'Reilly, S.Y., 1997. Volatile-bearing minerals and lithophile trace elements in the upper mantle. Chemical Geology 141, 153-184.

Ionov, D.A., Bodinier, J-L., Mukasa, S. B., Zanetti, A., 2002. Mechanism and sources of mantle metasomatism: major and trace element compositions of peridotite xenoliths from Spitsbergen in the context of numerical modelling. Journal of Petrology 43, 2219-2259.

1208 Ionov, D.A., 2007. Compositional variations and heterogeneity in fertile lithospheric mantle:
1209 peridotite xenoliths in basalts from Tariat, Mongolia. Contribution to Mineralogy and
1210 Petrology 154, 455-477.

1211 Ionov, D.A., Hofmann A. W., 2007. Depth of formation of subcontinental off-craton
1212 peridotites. Earth and Planetary Science Letters 261, 620–634.

1213 Ionov, D.A., 2010. Petrology of mantle wedge lithosphere: new data on supra-subduction
1214 zone peridotite xenoliths from the andesitic Avacha volcano, Kamchatka. Journal of
1215 Petrology 51, 327-361.

1216 Ionov, D.A., Bénard, A., Plechov, P.Yu., Shcherbakov, V.D., 2013. Along-arc variations in
1217 lithospheric mantle compositions in Kamchatka, Russia: First trace element data on
1218 mantle xenoliths from the Klyuchevskoy Group volcanoes. Journal of Volcanology
1219 and Geothermal Research 263, 122–131.

1220 Ishimaru, S., Arai, S., Ishida, Y., Mirasaka, M., Okrugin, V.M., 2007. Melting and Multi-
1221 stage Metasomatism in the MantleWedge beneath a Frontal Arc Inferred from Highly
1222 Depleted Peridotite Xenoliths from the AvachaVolcano, Southern Kamchatka. Journal
1223 of Petrology 48, 395-433.

1224 Ishimaru, S., Arai, S., 2008. Calcic amphiboles in peridotite xenoliths from Avacha volcano,
1225 Kamchatka, and their implications for metasomatic conditions in the mantle wedge.
1226 Geological Society Special Publications 293, 35-55.

1227 Lee, C.T., Rudnick, R.L., McDonough, W.F., Horn, I., 2000. Petrologic and geochemical
1228 investigation of carbonates in peridotite xenoliths from northeastern Tanzania.
1229 Contribution to Mineralogy and Petrology 139, 470-484.

1230 Lehmann, J., 1983. Diffusion between olivine and spinel: Application to geothermometry
1231 Earth and Planetary Science Letters, 64,123-138.

1232 Lustrino, M., Wilson, M., 2007. The circum-Mediterranean anorogenic Cenozoic igneous
1233 province. Earth-Science Reviews 81, 1–65.

1234 Mandler, B.E., Grove, T.L., 2016. Controls on the stability and composition of amphibole in
1235 the Earth's mantle. Contribution to Mineralogy and Petrology 171:68.

Martelli, M., Bianchini, G., Beccaluva, L., Rizzo, A., 2011. Helium and argon isotopic compositions of mantle xenoliths from Tallante and Calatrava, Spain. Journal of Volcanology and Geothermal Research 200, 18–26.

Martin, M., Wenzel, F., CALIXTO Working Group, 2006. High-resolution teleseismic body wave tomography beneath SE Romania: II. Imaging of a slab detachment scenario. Geophysical Journal International 164, 579–595.

Marty, B., 2012. The origins and concentrations of water, carbon, nitrogen and noble gases on Earth. Earth and Planetary Science Letters 313–314, 56–66.

Mason, P.R.D., Downes, H., Thirlwall, M. F., Seghedi, I., Szakács, A., Lowry, D., Mattey, D., 1996. Crustal assimilation as a major petrogenetic process in the East Carpathian Neogene and Quaternary continental margin arc, Romania. Journal of Petrology 37, 927-959.

Mason, P.R.D., Seghedi, I., Szákacs, A., Downes, H., 1998. Magmatic constraints on geodynamic models of subduction in the East Carpathians, Romania. Tectonophysics 297, 157–176.

Matenco, L., Bertotti, G., Leever, K., Cloetingh, S., Schmid, S.M., Tărăpoancă, M., Dinu, C., 2007. Large-scale deformation in a locked collisional boundary: Interplay between subsidence and uplift, intraplate stress, and inherited lithospheric structure in the late stage of the SE Carpathians evolution. Tectonics 26, TC4011, doi:10.1029/2006TC001951.

Mattioli, G.S., Wood, B., 1988. Magnetite activities across the $MgAl_2O_4$–Fe_3O_4 spinel join, with application to thermobarometric estimates of upper mantle oxygen fugacity. Contribution to Mineralogy and Petrology 98, 148–162.

McDonough, W.F., Sun, S.-S., 1995. The composition of the Earth. Chemical Geology 120, 223-253.

McInnes, B.I.A., Grégoire, M., Binns, R.A., Herzig, P.M., Hannington, M.D., 2001. Hydrous metasomatism of oceanic sub-arc mantle, Lihir, Papua New Guinea: petrology and geochemistry of fuid-metasomatised mantle wedge xenoliths. Earth and Planetary Science Letters 188, 169-183.

1265 Mercier, J.-C.C., Nicolas, A., 1975. Textures and fabrics of upper mantle peridotites as
1266 illustrated by xenoliths from basalts. Journal of Petrology 16, 454-487.

1267 Merten, S., Matenco, L., Foeken, J.P.T., Stuart, F.M., Andriessen, P.A.M., 2010. From
1268 nappe stacking to out-of-sequence post-collisional deformations: Cretaceous to
1269 Quaternary exhumation history of the SE Carpathians assessed by low-temperature
1270 thermochronology. Tectonics 29, TC3013.

1271 Moine, B.N., Grégoire, M., O'Reilly, S.Y., Sheppard, S.M.F., Cottin, J.Y., 2001. High field
1272 strength element fractionation in the upper mantle: evidence from amphibole-rich
1273 composite mantle xenoliths from the Kerguelen Islands (Indian Ocean). Journal of
1274 Petrology 42, 2145-2167.

1275 Molnár, K., Harangi, S., Lukács, R., Dunkl, I., Schmitt, A.K., Kiss, B., Garamhegyi, T.,
1276 Seghedi, I., 2018. The onset of the volcanismin the Ciomadul Volcanic Dome
1277 Complex (Eastern Carpathians): eruption chronology and magma type variation.
1278 Journal of Volcanology and Geothermal Research 354, 39–56.

1279 Moreira, M., Kunz, J., Allegre, C., 1998. Rare gas systematics in popping rock: Isotopic and
1280 elemental compositions in the upper mantle. Science 279, 1178–1181.

1281 Moreira, M., 2013. Noble gas constraints on the origin and evolution of earth's volatiles.
1282 Geochemical Perspectives 2, 229–230.

1283 Moreira, M., Rouchon, V., Muller, E., Noirez, S., 2018. The xenon isotopic signature of the
1284 mantle beneath Massif Central. Geochemical Perspective Letters 6, 28–32.

1285 Niu, Y., Langmuir, C.H., Kinzler, R.J., 1997. The origin of abyssal peridotites: a new
1286 perspective. Earth and Planetary Science Letters 152, 251-265.

1287 Niu, Y., 2004. Bulk-rock major and trace element compositions of abyssal peridotites:
1288 implications for mantle melting, melt extraction and post-melting processes beneath
1289 mid-ocean ridges. Journal of Petrology 45, 2423-2458.

1290 Ntaflos, T., Bizimis, M., Abart, R., 2017. Mantle xenoliths from Szentbékálla, Balaton:
1291 Geochemical and petrological constraints on the evolution of the lithospheric mantle
1292 underneath Pannonian Basin, Hungary. Lithos 276, 30-44.

1293 Oncescu, M.C., Burlacu, V., Anghel, M., Smalberger, V., 1984. Three-dimensional P-wave
1294 velocity image under the Carpathian arc. Tectonophysics 106, 305–319.

O'Neill, H. St.C., 1981. The transition between spinel lherzolite and garnet lherzolite and its use as a geobarometer. Contrib Mineral Petrol 77, 185 194.

Panaiotu, C.G., Pécskay, Z., Hambach, U., Seghedi, I., Panaiotu, C.C., Itaya, C.E.T., Orleanu, M., Szakács, A., 2004. Short-lived Quaternary volcanism in the Persani Mountains (Romania) revealed by combined K–Ar and paleomagnetic data. Geologica Carpathica 55, 333–339.

Parkinson, I.J., Arculus, R.J., Eggins, S.M., 2003. Peridotite xenoliths from Grenada, Lesser Antilles Island Arc. Contribution to Mineralogy and Petrology 146, 241–262.

Pécskay, Z., Edelstein, O., Seghedi, I., Szakács, A., Crihan, M., Bernad, A., 1995a. K-Ar dating of Neogene-Quaternary calc-alkaline volcanic rocks in Romania. Acta Vulcanologica 7, 53-61.

Pécskay, Z., Lexa, J., Szakács, A., Balogh, K., Seghedi, I., Konečný, V., Kovács, M., Márton, E., Kaličiak, M., Széky-Fux, V., Póka, T., Gyarmati, P., Edelstein, O., Rosu, E., Žec, B., 1995b. Space and time distribution of Neogene-Quaternary volcanism in the Carpatho-Pannonian Region. Acta Vulcanologica 7, 15-28.

Pilet, S., Ulmer, P., Villiger, S., 2010. Liquid line of descent of a basanitic liquid at 1.5 GPa: constraints on the formation of metasomatic veins. Contributions to Mineralogy and Petrology 159, 621–643.

Pouchou, J.L., Pichoir, F., 1991. Quantitative analysis of homogeneous or stratified microvolumes applied the model “PAP”, in: Heinrich, K.F.J., Newbury, D.E. (Eds.), Electron Probe Quantification. Plenum, New York, London, pp. 31–35.

Popa, M., Radulian, M., Szakács, A., Seghedi, I., Zaharia, B., 2012. New seismic and tomography data in the southern part of the Harghita Mountains (Romania, Southeastern Carpathians): connection with recent volcanic activity. Pure and Applied Geophysics 169, 1557–1573.

Rizzo, A.L., Pelorosso, B., Coltorti, M., Ntaflos, T., Bonadiman, C., Matusiak-Małek, M., Italiano, F., Bergonzoni, G., 2018. Geochemistry of noble gases and CO_2 in fluid inclusions from lithospheric mantle beneath Wilcza Góra (Lower Silesia, Southwest Poland). Frontiers in Earth Sciences 6:215. doi: 10.3389/feart.2018.00215.

1324 Roedder, E., 1984. Fluid inclusions reviews in mineralogy. Mineralogical Society of
1325 America 12, 644 doi: 10.1515/9781501508271.

1326 Sarda, P., Staudacher, T., and Allègre, C.J. (1988). Neon isotopes in submarine basalts.
1327 Earth and Planetary Science Letters 91, 73–88.

1328 Schmädicke, E., Gose, J., Will, T.M., 2011. Heterogeneous mantle underneath the North
1329 Atlantic: Evidence from water in orthopyroxene, mineral composition and equilibrium
1330 conditions of spinel peridotite from different locations at the Mid-Atlantic Ridge.
1331 Lithos 125, 308–320.

1332 Scott, J.M., Liu, J., Pearson, D.G., Waight T.E., 2016. Mantle depletion and metasomatism
1333 recorded in orthopyroxene in highly depleted peridotites. Chemical Geology 441, 280-
1334 291.

1335 Seghedi, I., Downes, H., Szakács, A., Mason, P.R.D., Thirlwall, M.F., Roşu, E., Pécskay, Z.,
1336 Marton, E., Panaiotu, C., 2004. Neogene-Quaternary magmatism and geodynamics in
1337 the Carpathian–Pannonian region: a synthesis. Lithos 72, 117–146.

1338 Seghedi, I., Matenco, L., Downes, H., Mason, P.R.D., Szakács, A., Pécskay, Z., 2011.
1339 Tectonic significance of changes in post-subduction Pliocene-Quaternary magmatism
1340 in the south east part of the Carpathian–Pannonian region. Tectonophysics 502, 146–
1341 157.

1342 Seghedi, I., Downes, H., 2011. Geochemistry and tectonic development of Cenozoic
1343 magmatism in the Carpathian–Pannonian region. Gondwana Research, 20, 655–672.

1344 Seghedi, I., Popa R-G., Panaiotu, C.G., Szakács, A., Pécskay, Z., 2016. Short-lived eruptive
1345 episodes during the construction of a Na-alkalic basaltic field (Perşani Mountains, SE
1346 Transylvania, Romania). Bullettin of Volcanology 78:69, DOI 10.1007/s00445-016-
1347 1063-y.

1348 Seyler, M., Cannat, M.C., Mével, C., 2003. Evidence for major-element heterogeneity in the
1349 mantle source of abyssal peridotites from the Southwest Indian Ridge (52° to 68°E).
1350 Geochemistry Geophysics Geosystems 4, 9101, DOI:10.1029/2002GC000305.

1351 Shibata, T., Thompson, G., 1986. Peridotites from the Mid-Atlantic Ridge at 43° N and their
1352 petrogenetic relation to abyssal tholeiites. Contributions to Mineralogy and Petrology
1353 93,144-159.

1354 Sorbadere F., Laurenz V., Frost D.J., Wenz M., Rosenthal A., McCammon C., Rivard C.,
1355 2018. The behaviour of ferric iron during partial melting of peridotite. Geochimica et
1356 Cosmochimica Acta 239, 235–254.

1357 Straub, S. M., Gomez-Tuena, A., Stuart, F.M., Zellmer, G.F., Espinasa-Perena, R., Cai, Y.,
1358 Iizuka, Y., 2011. Formation of hybrid arc andesites beneath thick continental crust.
1359 Earth and Planetary Science Letters 303, 337-347.

1360 Szabó, Cs., Vaselli, O., Vanucci, R., Bottazzi, P., Ottolini, L., Coradossi, N., Kubovics, I.,
1361 1995a. Ultramafic xenoliths from the Little Hungarian Plain (Western Hungary): a
1362 petrologic and geochemical study. Acta Vulcanologica 7, 249–263.

1363 Szabó, C., Harangi, S., Vaselli, O., Downes, H., 1995b. Temperature and oxygen fugacity in
1364 peridotite xenoliths from the Carpathian-Pannonian Region. Acta Vulcanologica 7,
1365 231-239.

1366 Szakács, A., Seghedi, I., Pécskay, Z. 1993. Pecularities of South Harghita Mts. as terminal
1367 segment of the Carpathian Neogene to Quaternary volcanic chain. Revue Roumaine de
1368 Géologie 37, 21–36.

1369 Szakács, A., Seghedi, I., 1995. The Călimani-Ghiurghiu-Harghita volcanic chain, East
1370 Carpathians, Romania: volcanological features. Acta Vulcanologica 7, 145-153.

1371 Takazawa, E., Frey, F.A., Shimizu, N., Obata, M., 2000. Whole rock compositional
1372 variation in an upper mantle peridotite (Horoman, Hokkaido, Japan): are they
1373 consistent with a partial melting process. Geochimica et Cosmochimica Acta 64, 695–
1374 716.

1375 Taylor, W.R. 1998. An experimental test of some geothermometer and geobarometer
1376 formulations for upper mantle peridotites with application to the thermobarometry of
1377 fertile lherzolite and garnet websterite. Neues Jahrbuch für Mineralogie Abhandlungen
1378 172, 381-408.

1379 Tiepolo, M., Bottazzi, P., Palenzona, M., Vannucci, R., 2003. A Laser probe coupled with
1380 ICP double-focusing sector-field mass spectrometer for in situ analysis of geological
1381 samples and U–Pb dating of zircon. The Canadian Mineralogist 41, 259–272.

1382 Touron, S., Renac, C., O'Reilly, S.Y., Cottin, J.-Y., Griffin, W.L., 2008. Characterization of
1383 the metasomatic agent in mantle xenoliths from Devès, Massif Central (France) using

coupled in situ trace-element and O, Sr and Nd isotopic compositions, in: Coltorti M., Grégoire M. (Eds) "Metasomatism in Oceanic and Continental Lithospheric Mantle". Geological Society, London, Special Publication 293, pp 177-196.

Trull, T.W., Kurz, M.D., 1993. Experimental measurements of ^{3}He and ^{4}He mobility in olivine and clinopyroxene at magmatic temperatures. Geochimica et Cosmochimica Acta 57, 1313–1324.

Upton, B.G.J., Downes, H., Bonadiman, C., Kirstein, L.A., Hill, P.G., Ntaflos, T., 2011. The lithospheric mantle and lower crust-mantle relationships under Scotland: a xenolithic perspective. Journal of the Geological Society, London 168, 873-885.

Vaselli, O., Downes, H., Thirlwall, M.F., Dobosi, G., Coradossi, N., Seghedi, I., Szakács, A., Vannucci, R., 1995. Ultramafic xenoliths in Plio-Pleistocene alkali basalts from the Eastern Transylvanian basin: depleted mantle enriched by vein metasomatism. Journal of Petrology 36, p.23-55.

Vaselli, O., Minissale, A., Tassi, F., Magro, G., Seghedi, I., Ioane, D., Szakács, A., 2002. A geochemical traverse across the Eastern Carpathians (Romania): constraints on the origin and evolution of the mineral waters and gas discharge. Chemical Geology 182, 637–654.

Zanetti, A., Vannucci, R., Oberti, R., Dobosi, G., 1995. Trace-element composition and crystal-chemistry of mantle amphiboles from the Carpatho-Pannonian region. Acta Vulcanologica 7, 265-276.

Ziberna, L., Klemme, S., Nimis, P., 2013. Garnet and spinel in fertile and depleted mantle: insights from thermodynamic modelling. Contribution to Mineralogy and Petrology 166, 411–421.

Witt-Eickschen, G., Harte, B., 1994. Distribution of trace elements between amphibole and clinopyroxene from mantle peridotites of the Eifel (western Germany): An ion-microprobe study. Chemical Geology 117, 235-250.

Witt-Eickshen, G., Kaminsky, W., Kramm, U., Harte, B., 1998. The nature of young vein metasomatism in the lithosphere of the West Eifel (Germany): geochemical and isotopic constraints from composite mantle xenoliths from the Meerfelder Maar. Journal of Petrology 39, 155-185.

Wood, B.J., Virgo, D., 1989. Upper mantle oxidation state: ferric iron contents of lherzolite spinels by ^{57}Fe Mössbauer spectroscopy and resultant oxygen fugacities. Geochimica et Cosmochimica Acta 53, 1227–1291.

Workman, R.K., Hart, S.R., 2005. Major and trace element composition of the depleted MORB mantle (DMM). Earth and Planetary Science Letters 231, 53-72.

Yamamoto, J., Kaneoka, I., Nakai, S., Kagi, H., Prikhod'ko, V.S., Arai, S., 2004. Evidence for subduction-related components in the subcontinental mantle from low ^{3}He/^{4}He and ^{40}Ar/^{36}Ar ratio in mantle xenoliths from Far Eastern Russia. Chemical Geology 207, 237–259.

Yamamoto, J., Nishimura, K., Sugimoto, T., Takemura, K., Takahata, N., Sano, Y., 2009. Diffusive fractionation of noble gases in mantle with magma channels: origin of low He/Ar in mantle-derived rocks. Earth and Planetary Science Letters 280, 167–174.

Yoshikawa, M., Tamura, A., Arai, S., Kawamoto, T., Payot, B.D., Rivera, D.J., Bariso, E.B., Mirabueno, M.H.T., Okuno, M., Kobayashi, T., 2016. Aqueous fluids and sedimentary melts as agents for mantle wedge metasomatism, as inferred from peridotite xenoliths at Pinatubo and Iraya volcanoes, Luzon arc, Philippines. Lithos 262, 355-368.

FIGURE CAPTIONS

Fig. 1. Geological sketch of Pannonian Basin and volcanological map of Perşani Mountains in the Transylvanian Basin. C-G-H indicates the Calimani-Ghiurghiu-Harghita volcanic arc. The mantle xenolith sampling sites (LAG-BARC-TRE) are also indicated, corresponding to loose pyroclastic deposits of La Gruiu volcanic center and along Barc and Trestia creeks, respectively.

Fig. 2: Mg# vs Al_2O_3 (A) and TiO_2 (B) and Al_2O_3 vs Na_2O (C) of primary cpx and mg# vs Al_2O_3 (D) of all cpx (both primary and secondary) in PMVF mantle xenoliths. (a), anhydrous samples. Black square ("PM calc"), PM cpx composition calculated through mass balance from Bulk Silicate Earth of McDonough and Sun (1995) and Johnson et al. (1990) modes. Thick line in (A) and (D),

cpx melting model according to Bonadiman and Coltorti (2019). Small grey dots, PMVF cpx data from Vaselli et al. (1995). Primary cpx (black asterisks) from Pacific arc mantle wedge xenoliths (Abe et al., 1998; Mc Innes et al., 2001; Brandon and Draper, 1996; Kepezhinskas et al., 1996; Arai et al., 2004; Bryant and Yogodzinsky, 2007; Ishimaru et al., 2007) are also reported for comparison in (A).

Fig. 3. Mg# vs Al_2O_3 (A) and CaO (B) of opx in PMVF mantle xenoliths, divided by textural sub-groups. (a), anhydrous samples. Black square ("PM calc"), PM opx composition calculated through mass balance from Bulk Silicate Earth of McDonough and Sun (1995) and Johnson et al. (1990) modes. Thick line, opx melting model according to Bonadiman and Coltorti (2019). Small grey dots, PMVF opx data from Vaselli et al. (1995). Primary (black asterisks) and secondary (violet crosses) opx from Pacific arc mantle wedge xenoliths (Brandon and Draper, 1996; Kepezhinskas et al., 1996; Arai et al., 2003, 2004; Bryant and Yogodzinsky, 2007; Ishimaru et al., 2007) are also reported for comparison.

Fig. 4. Mg# vs Al_2O_3 (A) and TiO_2 (B) of disseminated (amph-D) and vein (amph-V) amphiboles in PMVF mantle xenoliths, divided by textural sub-groups. Small grey dots, asterisks and squares are disseminated amphiboles, vein amphiboles and amphiboles in clinopyroxenites in PMVF ultramafic xenoliths reported by Vaselli et al. (1995). Small black crosses, amphibole megacrystals (MXC) found in Persani Mts pyroclastic deposits by Downes et al. (1995) and Zanetti et al. (1995).

Fig. 5. Mg# vs cr# of primary spinel in PMVF mantle xenoliths, divided by textural sub-groups. (a), anhydrous samples. Black square ("PM calc"), PM spinel composition calculated through mass balance from Bulk Silicate Earth of McDonough and Sun (1995) and Johnson et al. (1990) modes. Small grey dots, PMVF spinel data from Vaselli et al. (1995).

Fig. 6. Chondrite normalized REE (A, C, E) and trace element (B, D, F) patterns of cpx in PMVF mantle xenoliths, divided in three Groups according to their geochemical features (see text for further explanations). Average patterns of disseminated amphibole associated to the different cpx Groups (black dotted lines) are also reported for comparison.

Fig. 7. Chondrite normalized REE (A, C, E) and trace element (B, D, F) patterns of opx in PMVF mantle xenoliths, divided in three Groups according to their geochemical features (see text for further explanations).

Fig. 8. Chondrite normalized REE (A, C, E) and trace element (B, D, F) patterns of amphibole in PMVF mantle xenoliths, divided in three Groups according to their geochemical features (see text for further explanations). Average patterns of the associated different cpx Groups (black dotted lines) are also reported for comparison. The pattern with asterisk symbol represents LAG52 vein amphibole.

Fig. 9. Diagram of $^{21}Ne/^{22}Ne$ versus $^{20}Ne/^{22}Ne$ measured in fluid inclusions of PMVF xenoliths. Olivine abbreviated as "ol". The black dashed and dotted lines represent binary mixing between air ($^{21}Ne/^{22}Ne = 0.0290$ and $^{20}Ne/^{22}Ne = 9.8$) and i) MORB mantle as defined by Sarda et al. (1988) and Moreira et al. (1998) at $^{21}Ne/^{22}Ne = 0.06$ and $^{20}Ne/^{22}Ne = 12.5$; ii) CRUST as defined by Ballentine (1997) and references therein at $^{21}Ne/^{22}Ne = 0.6145$ (mean of 0.469-0.76) and $^{20}Ne/^{22}Ne = 0.3$; iii) SOLAR WIND as defined by Heber et al. (2009) at $^{21}Ne/^{22}Ne = 0.0328$ and $^{20}Ne/^{22}Ne = 13.8$. Data from other European localities are also reported (French Massif Central, Eifel, and Kapfenstein in Pannonian Basin, Gautheron et al., 2005; Calatrava and Tallante, Martelli et al., 2011; Lower Silesia, Rizzo et al., 2018).

Fig. 10. Concentrations of a) ^{4}He and b) $^{40}Ar^{*}$ versus $^{3}He/^{4}He$ corrected for air contamination (Rc/Ra values). Olivine abbreviated as "ol". The blue bar indicates the range of $^{3}He/^{4}He$ ratios for a MORB-like mantle (8±1 Ra; Graham, 2002). The two diffusive fractionation paths are modeled based on the approach of Burnard et al. (1998), Burnard (2004) and Yamamoto et al. (2009), taking into account the diffusion coefficient (D) of ^{3}He, ^{4}He, and $^{40}Ar^{*}$ (D_{3He}/D_{4He} = 1.15 and D_{4He}/D_{40Ar} = 3.16 in solid mantle; Trull and Kurz, 1993; Burnard, 2004; Yamamoto et al., 2009). Starting and final conditions as well as further details on modeling are reported in the text (Section 6.3.2). Data from other European localities as in Fig. 9 caption.

Fig. 11. a) $^{3}He/^{36}Ar$ and b) ^{4}He (mol/g) versus $^{40}Ar/^{36}Ar$. Olivine abbreviated as "ol". The continuous and dashed turquoise lines represent binary mixing between air [$^{40}Ar/^{36}Ar$ = 295.5, $^{3}He/^{36}Ar = 2.3\times10^{-7}$ and $^{4}He = 1.1\times10^{-16}$ (arbitrarily fixed to fit data)] and MORB mantle as defined by Burnard et al. (1997), Moreira et al. (1998), and Ballentine et al. (2005) at $^{40}Ar/^{36}Ar$ = 44,000, $^{3}He/^{36}Ar$ = 0.49 and $^{4}He = 1.0\times10^{-10}$ (arbitrarily fixed to fit data), considering $^{3}He/^{4}He$ = 8, $^{4}He/^{40}Ar^{*}$ = 1 and $^{4}He/^{40}Ar^{*}$ = 0.1. Data from other European localities as in Fig. 9 caption.

Fig. 12. $^{4}He/^{40}Ar^{*}$ versus $^{3}He/^{4}He$ corrected for air contamination (Rc/Ra values). Olivine abbreviated as "ol". The blue rectangle indicates MORB ($^{3}He/^{4}He$ = 8±1 Ra; Graham, 2002; $^{4}He/^{40}Ar^{*}$ = 1–5; Marty, 2012). The two diffusive fractionation paths are modeled as reported in Fig. 10 and in Section 6.3.2. Data from other European localities as in Fig. 9 caption.

Fig. 13. Discrimination diagrams for amphibole geodynamic affinity by Coltorti et al. (2007). I-amph and S-amph indicate Intraplate amphibole and Subductive amphibole, respectively. Amph-V and MXC are the composition of PMVF vein amphibole and Perşani Mts. megacrystals, respectively, as reported by Zanetti et al. (1995).

Fig. 14. Chondrite-normalized, average REE patterns of PMVF disseminated amphibole (symbols as in Fig. 8, abbreviations as in Fig. 4) and LAG52 vein amphibole (PMVF amph-V) compared to literature data of PMVF vein amphibole (pink shaded field, Zanetti et al., 1995; Vaselli et al., 1995; Chalot-Prat and Boullier, 1997) and Perşani Mts. megacrystals (MXC, grey asterisks, Downes et al., 1995; Zanetti et al., 1995). Red and cyan triangles are megacrystal compositions representing frozen alkaline melts at open and closed system conditions, according to Zanetti et al. (1995).

Fig. 15. Chondrite-normalized REE patterns of the calculated melt in equilibrium with LAG52 amphibole vein (yellow dots) and the calculated cpx (red diamonds) in equilibrium with this melt. Frozen alkaline metasomatic melt according to Zanetti et al. (1995) (cyan triangles), composition of cpx in a PMVF clinopyroxenite (pink diamonds, Chalot-Prat and Boullier, 1997), average PMVF disseminated cpx (symbols as in Fig. 6) and Perşani Mts. lavas (Downes et al., 1995; Harangi et al., 2013) are reported for comparison.

Figure 1

Click here to download high resolution image

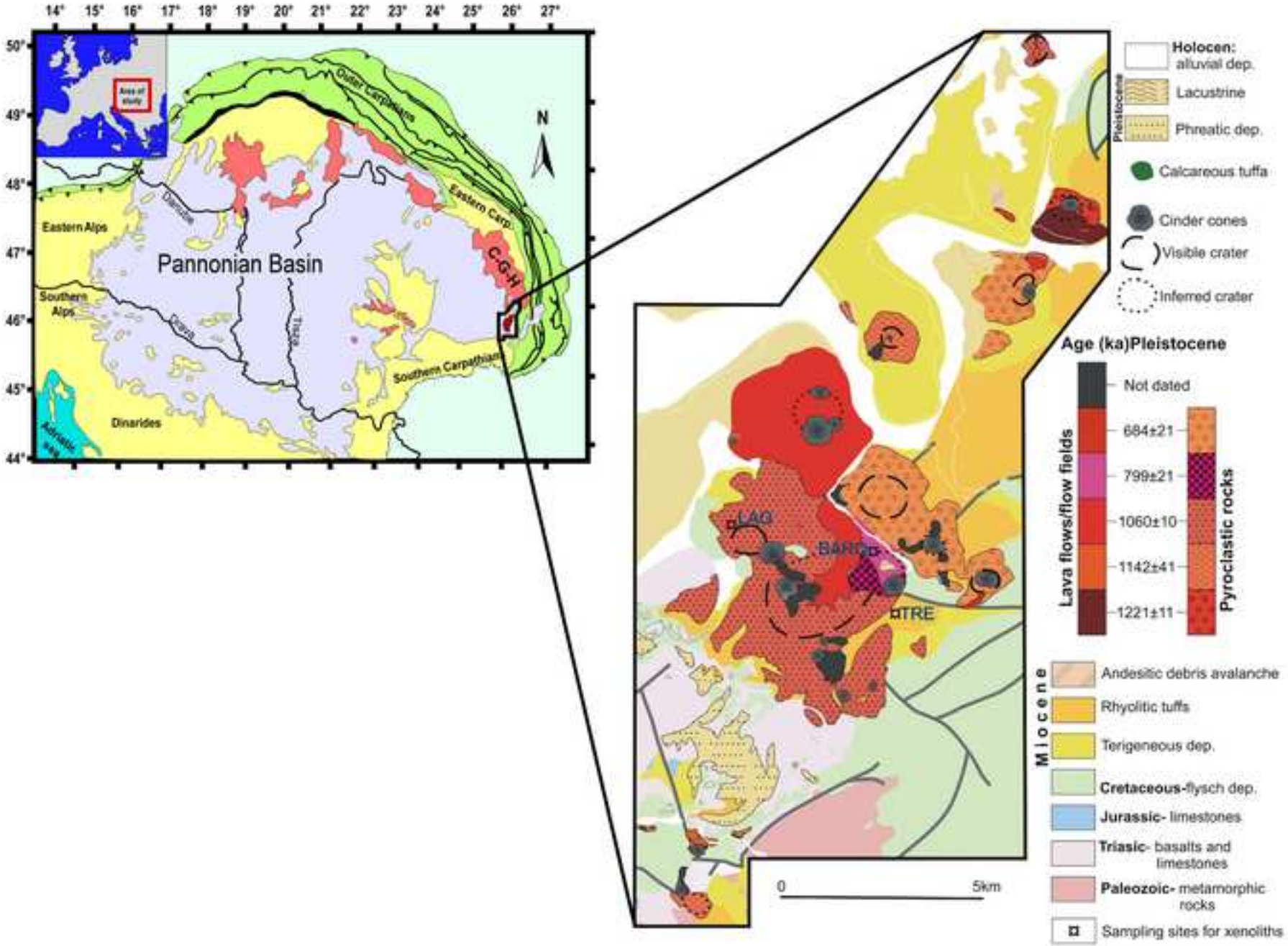

Figure 2

Click here to download high resolution image

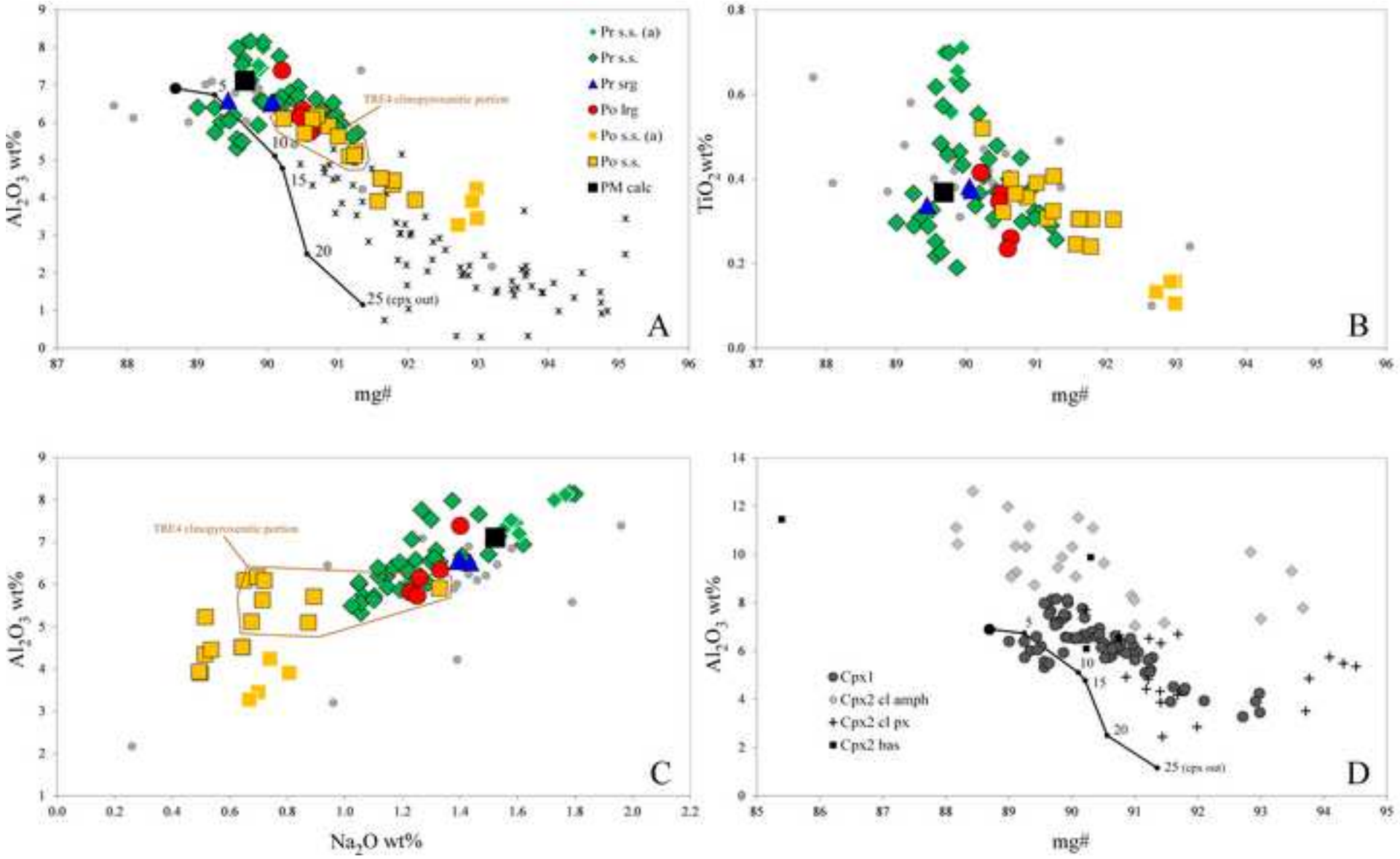

Figure 3

Click here to download high resolution image

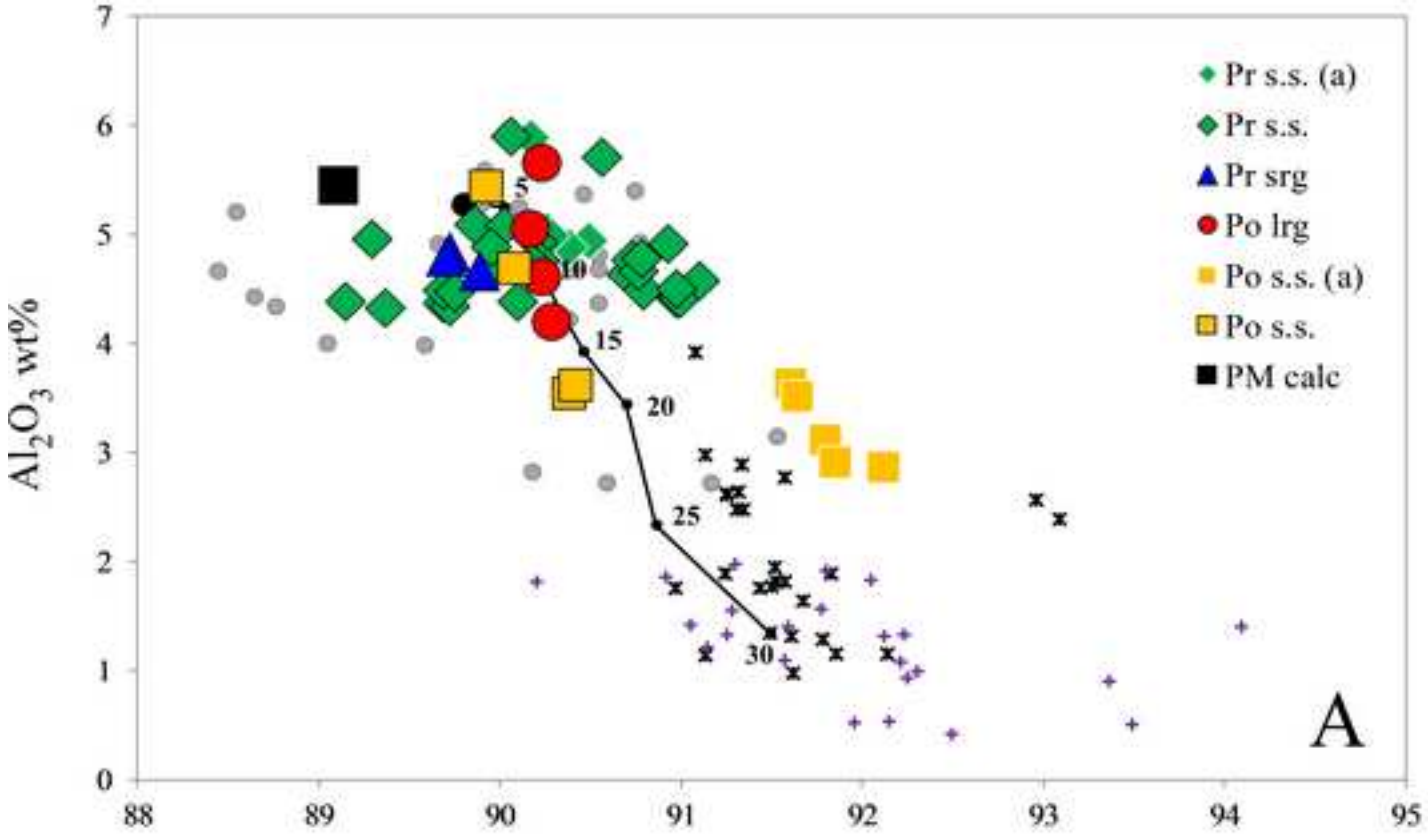

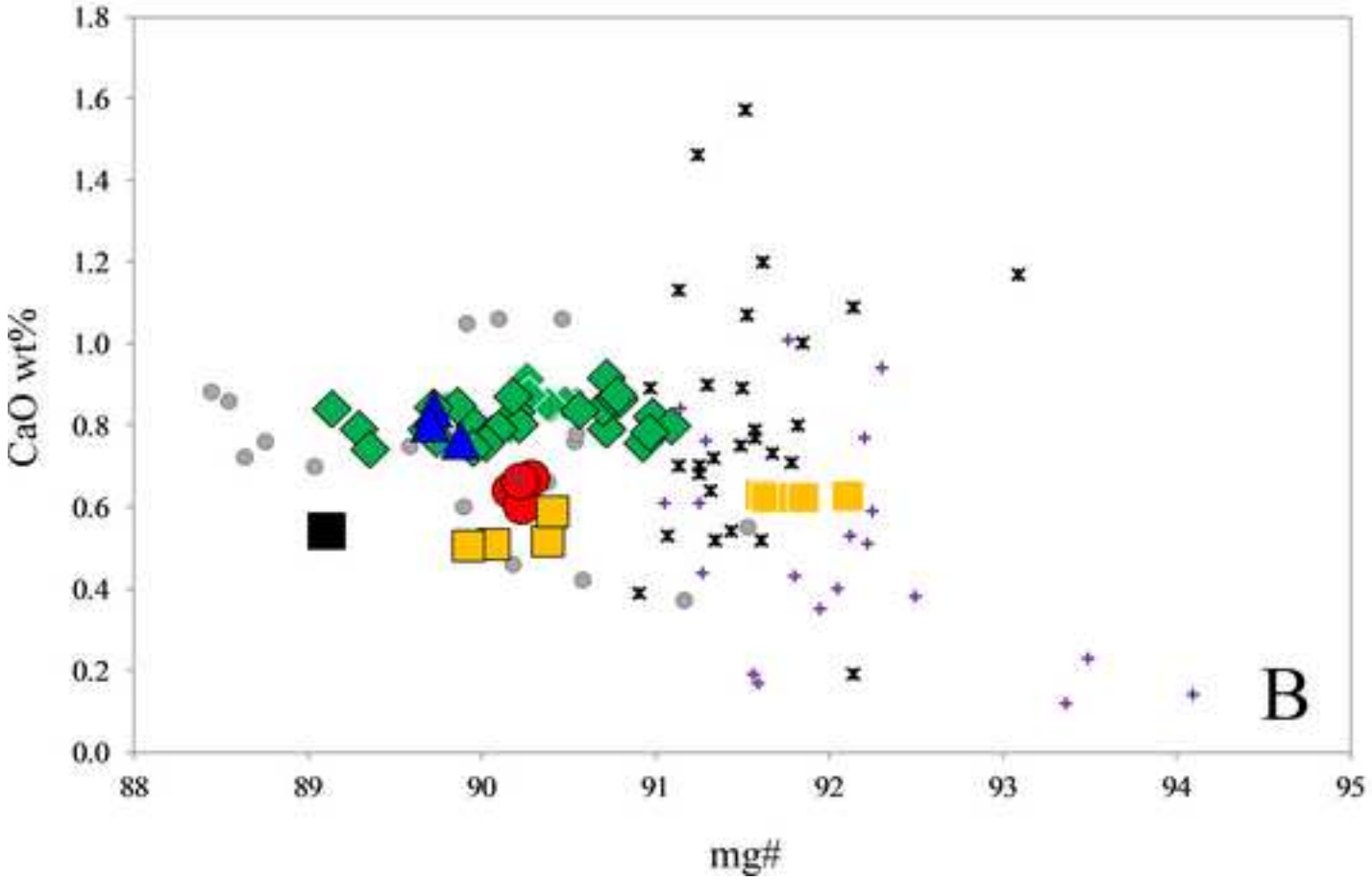

Figure 4

Click here to download high resolution image

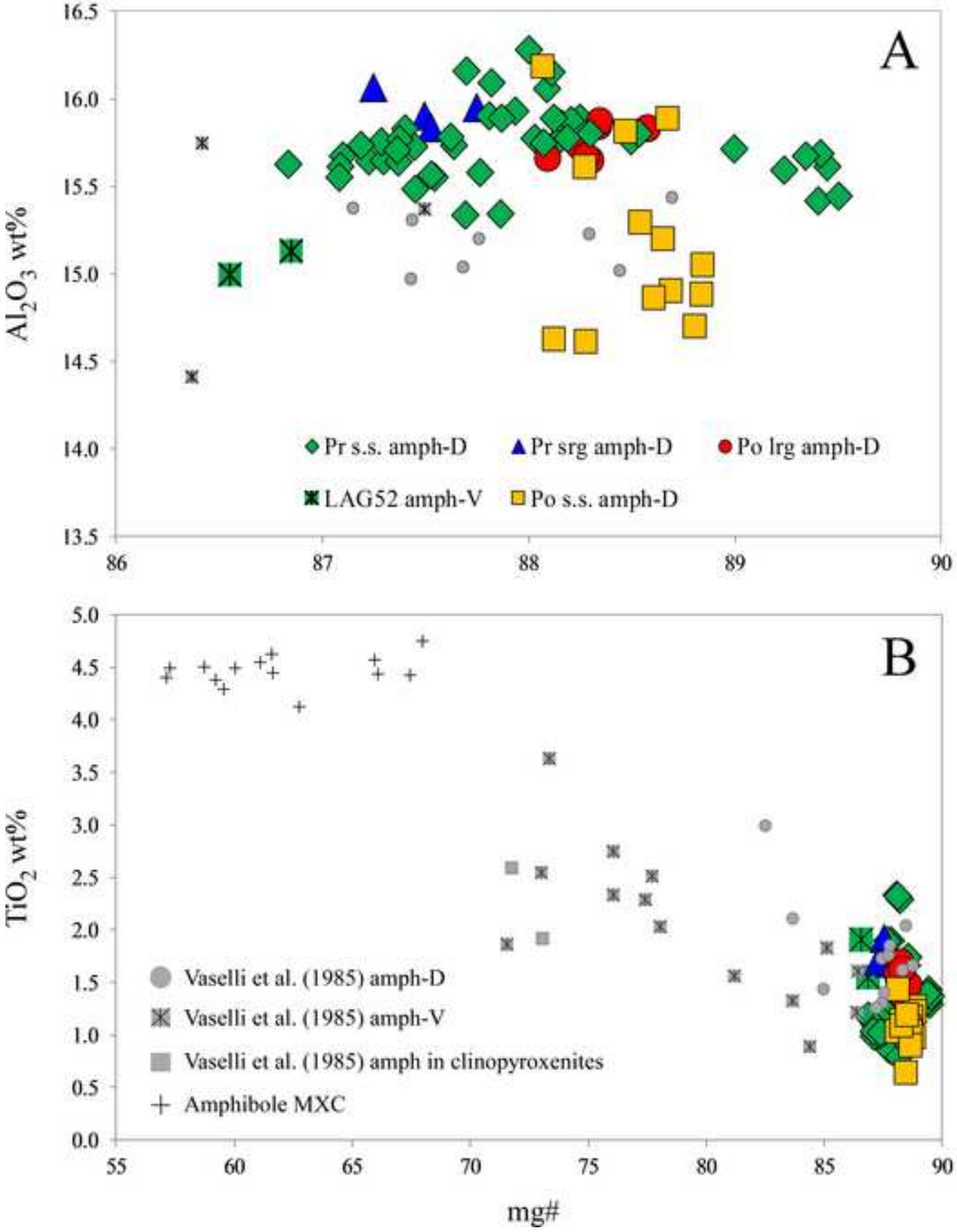

Figure 5

Click here to download high resolution image

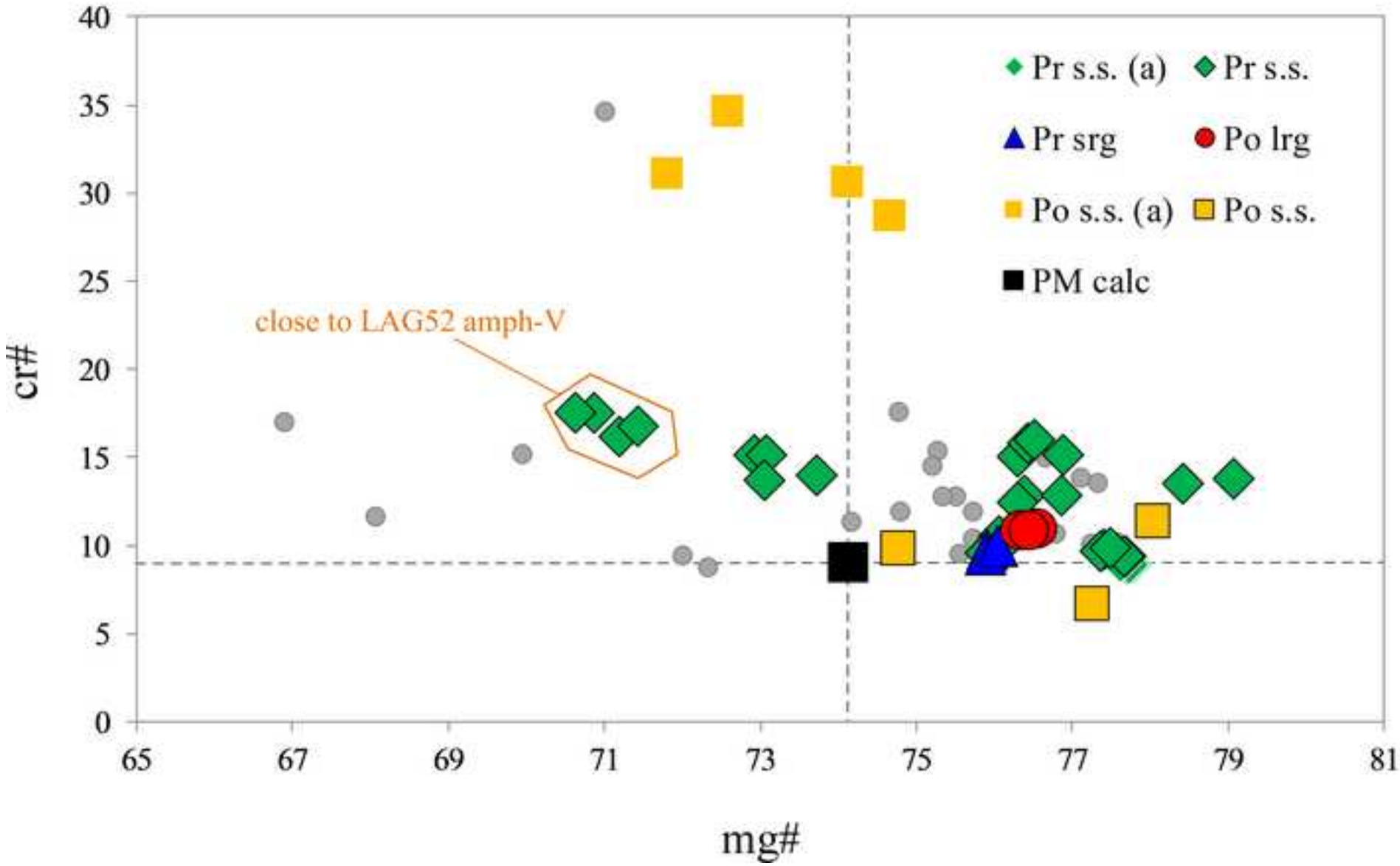

Figure 6

Click here to download high resolution image

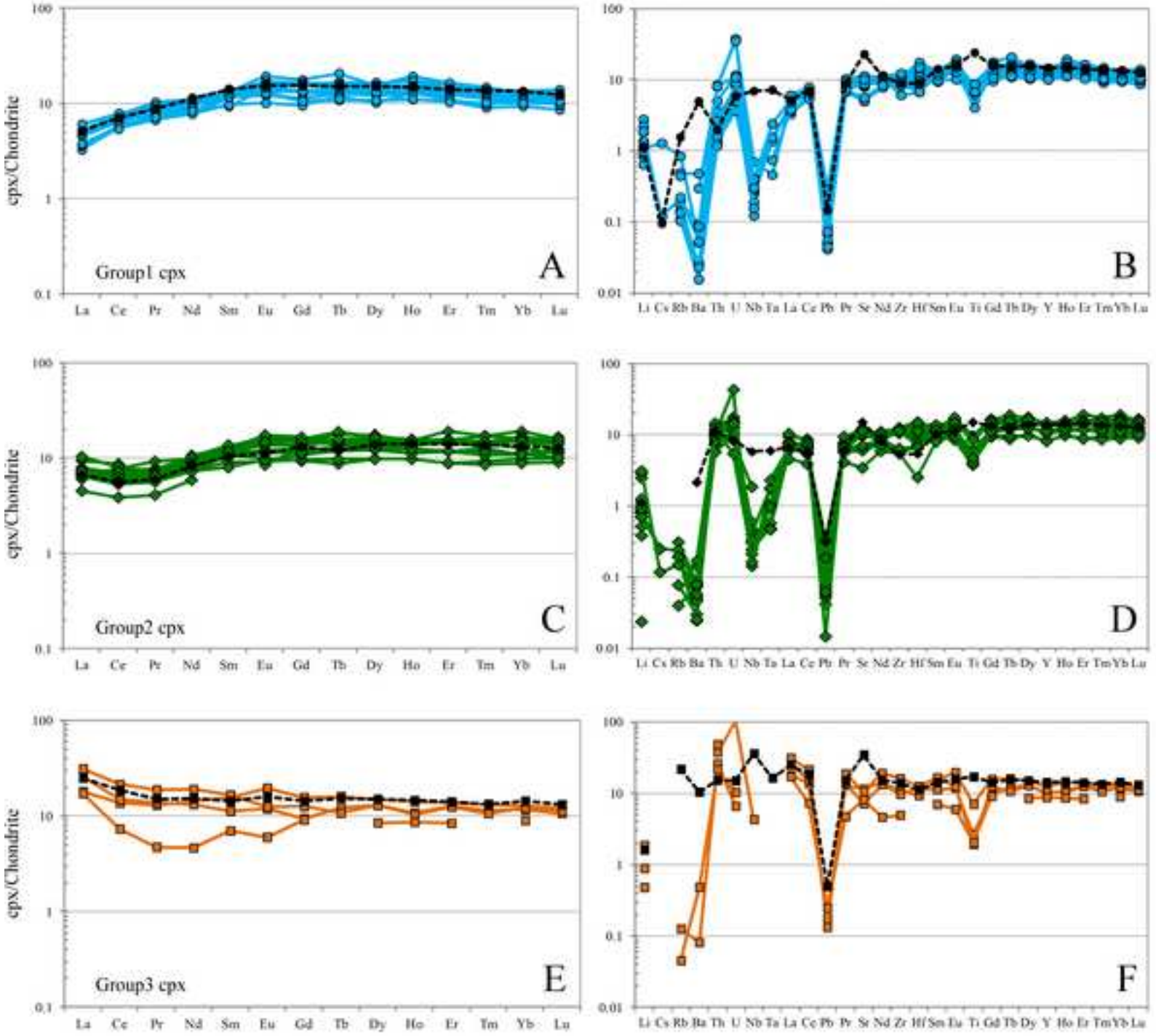

Figure 7

Click here to download high resolution image

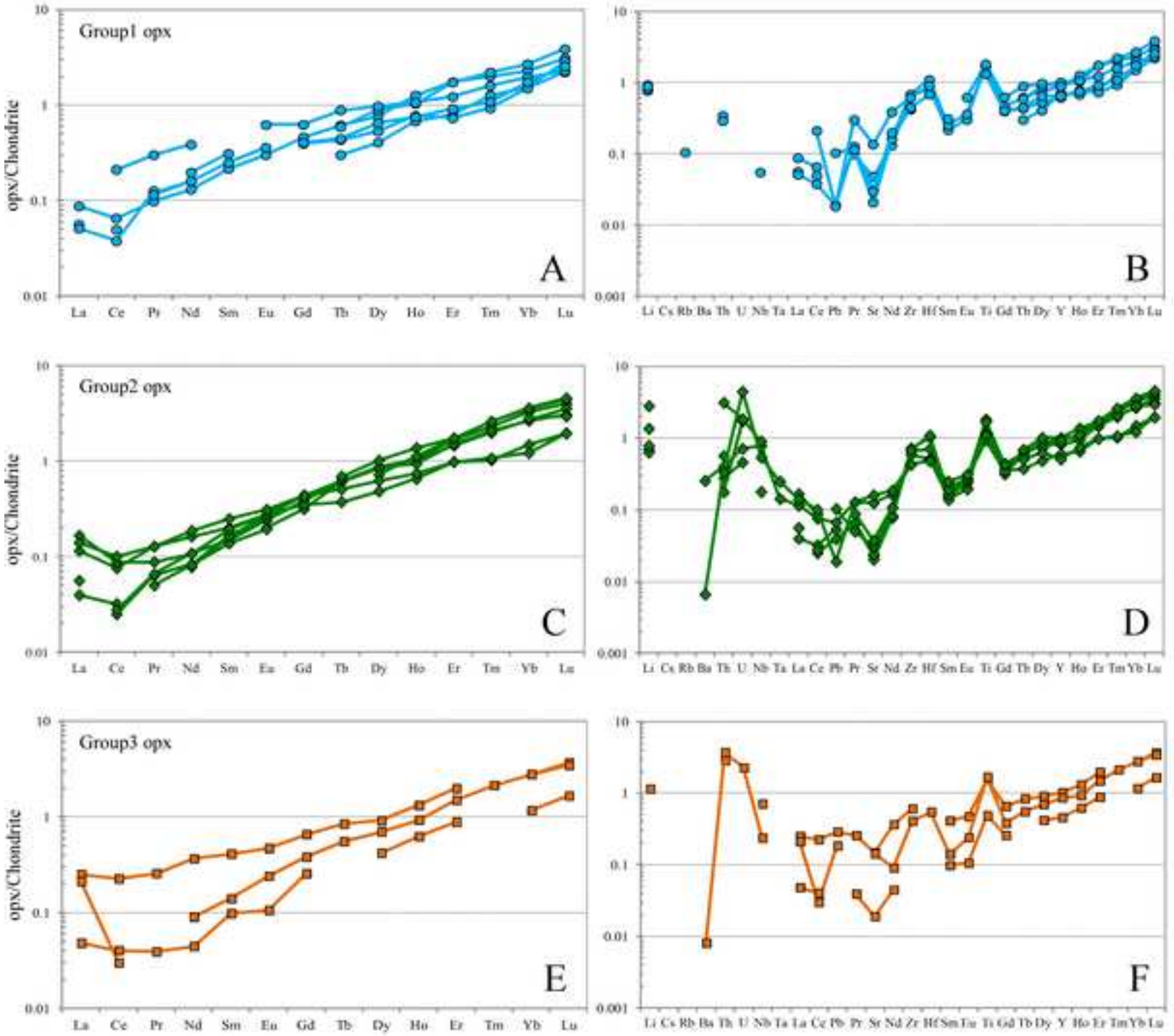

Figure 8

Click here to download high resolution image

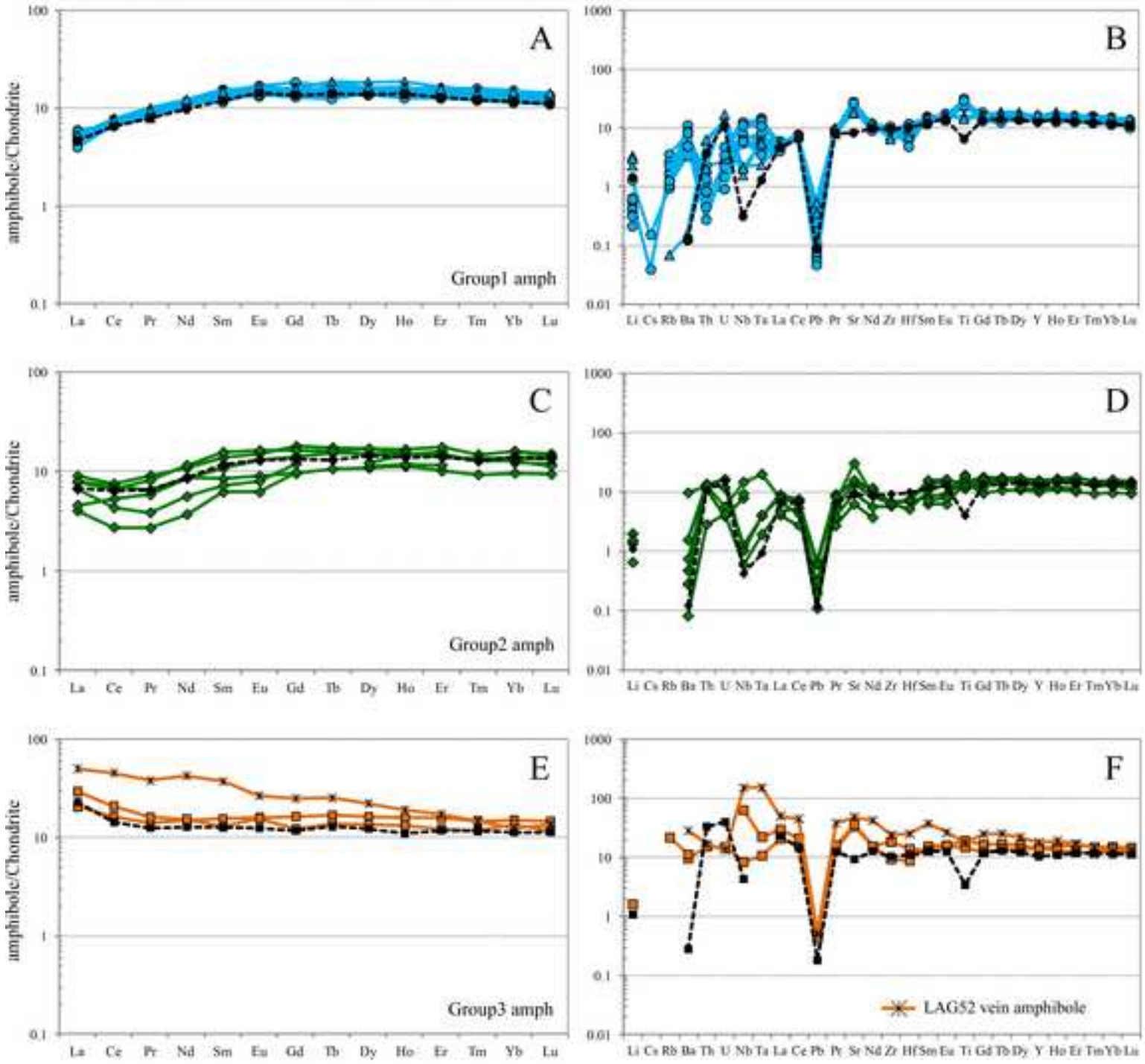

Figure 9

Click here to download high resolution image

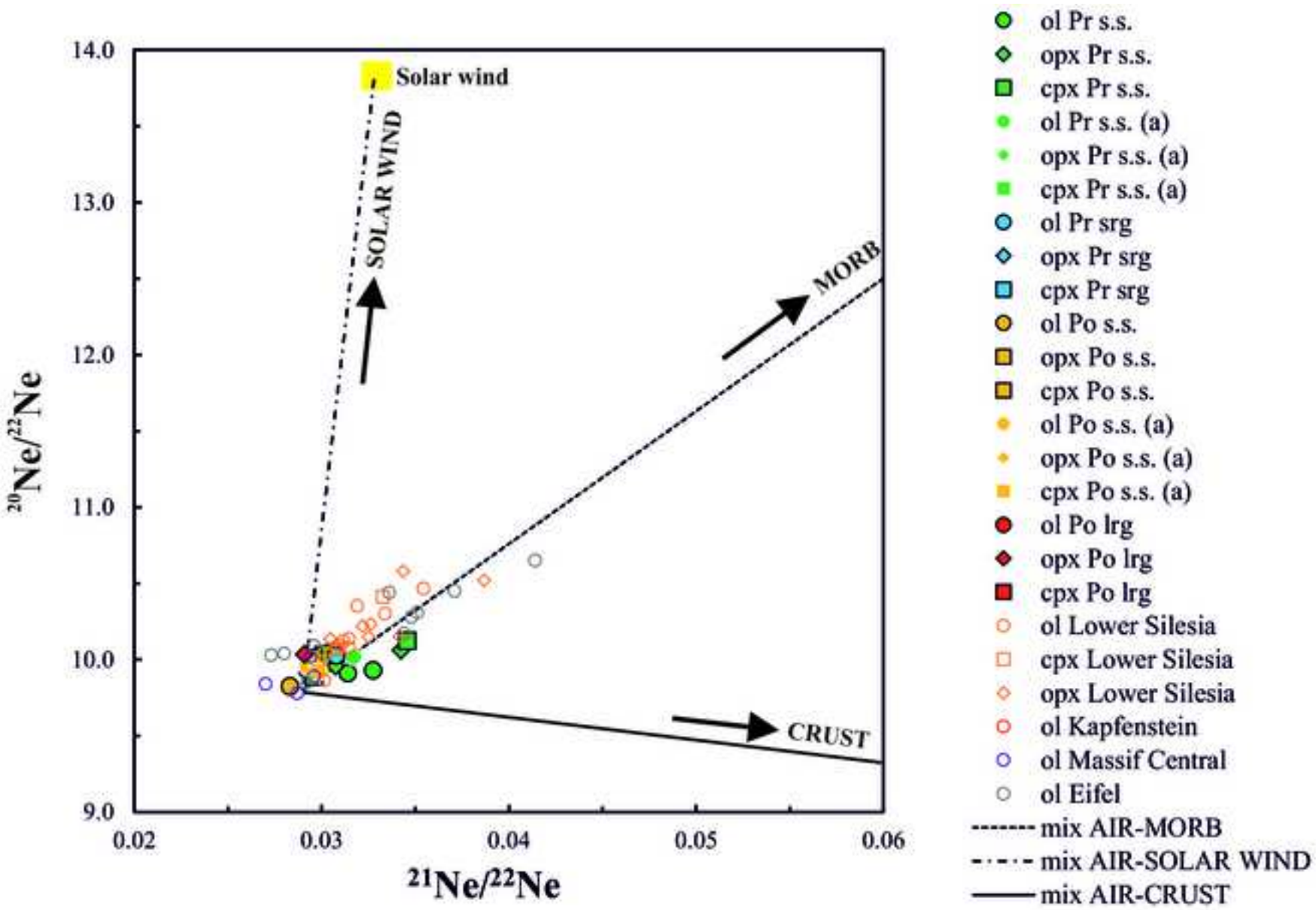

Figure 10

Click here to download high resolution image

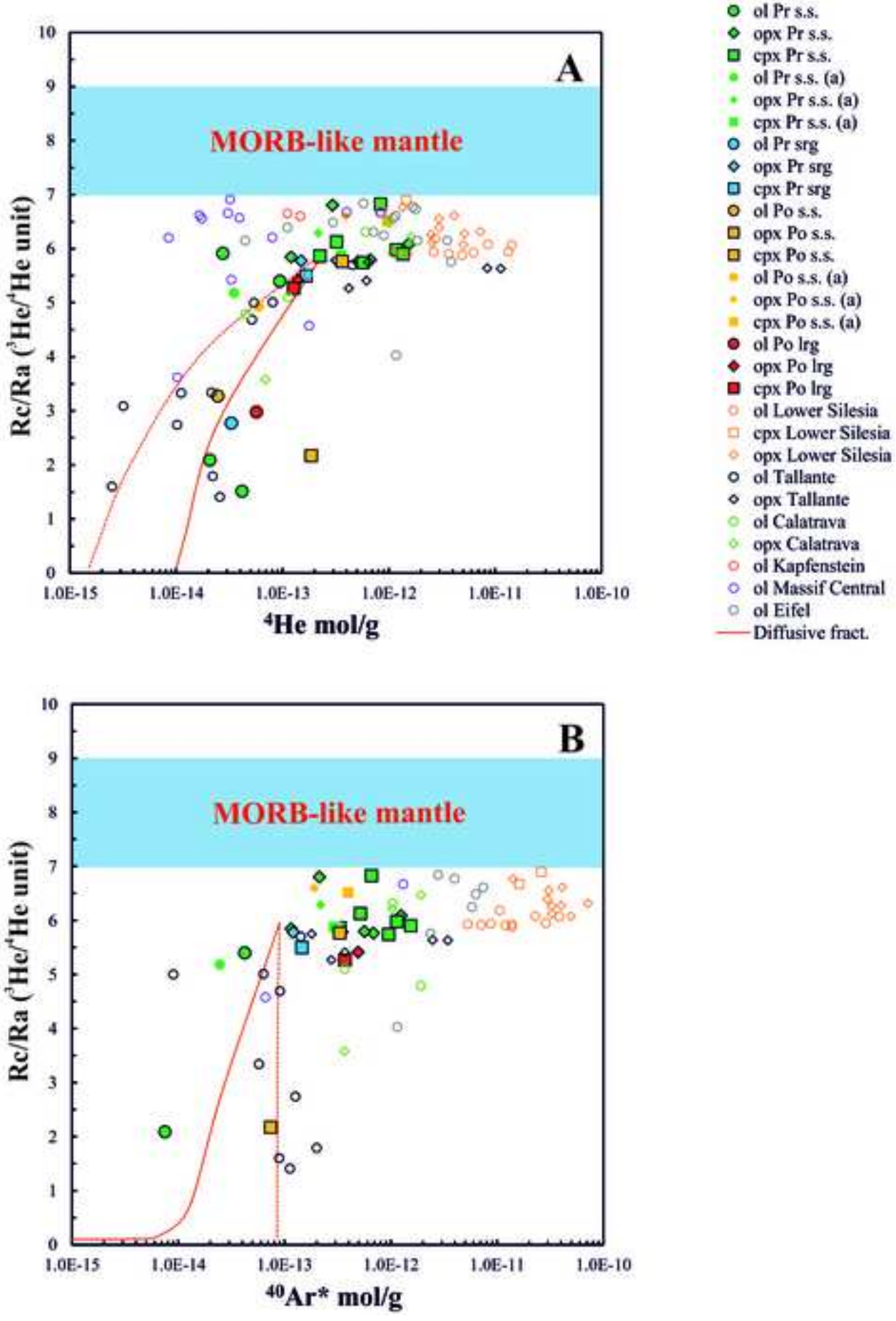

Figure 11

Click here to download high resolution image

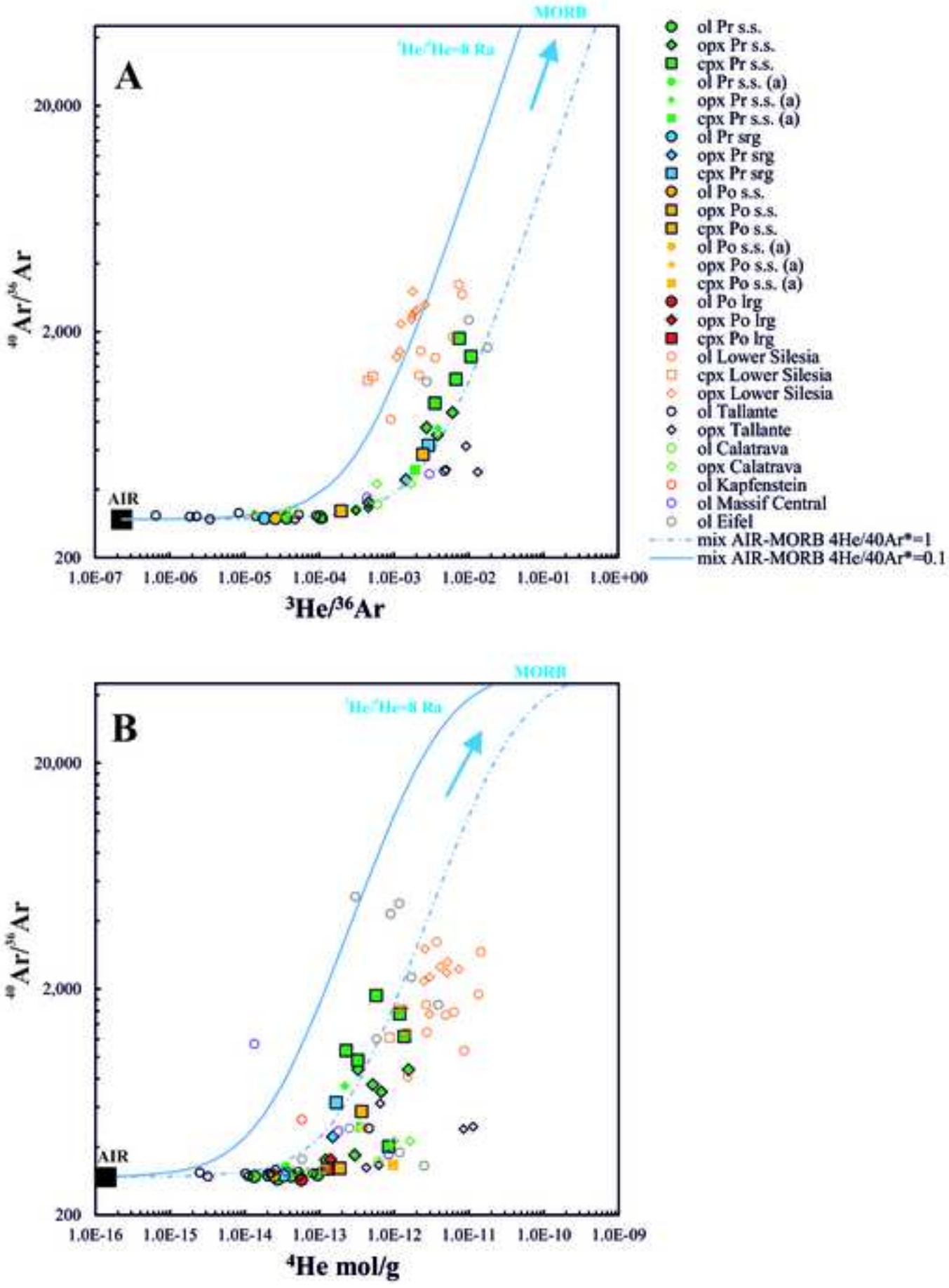

Figure 12

Click here to download high resolution image

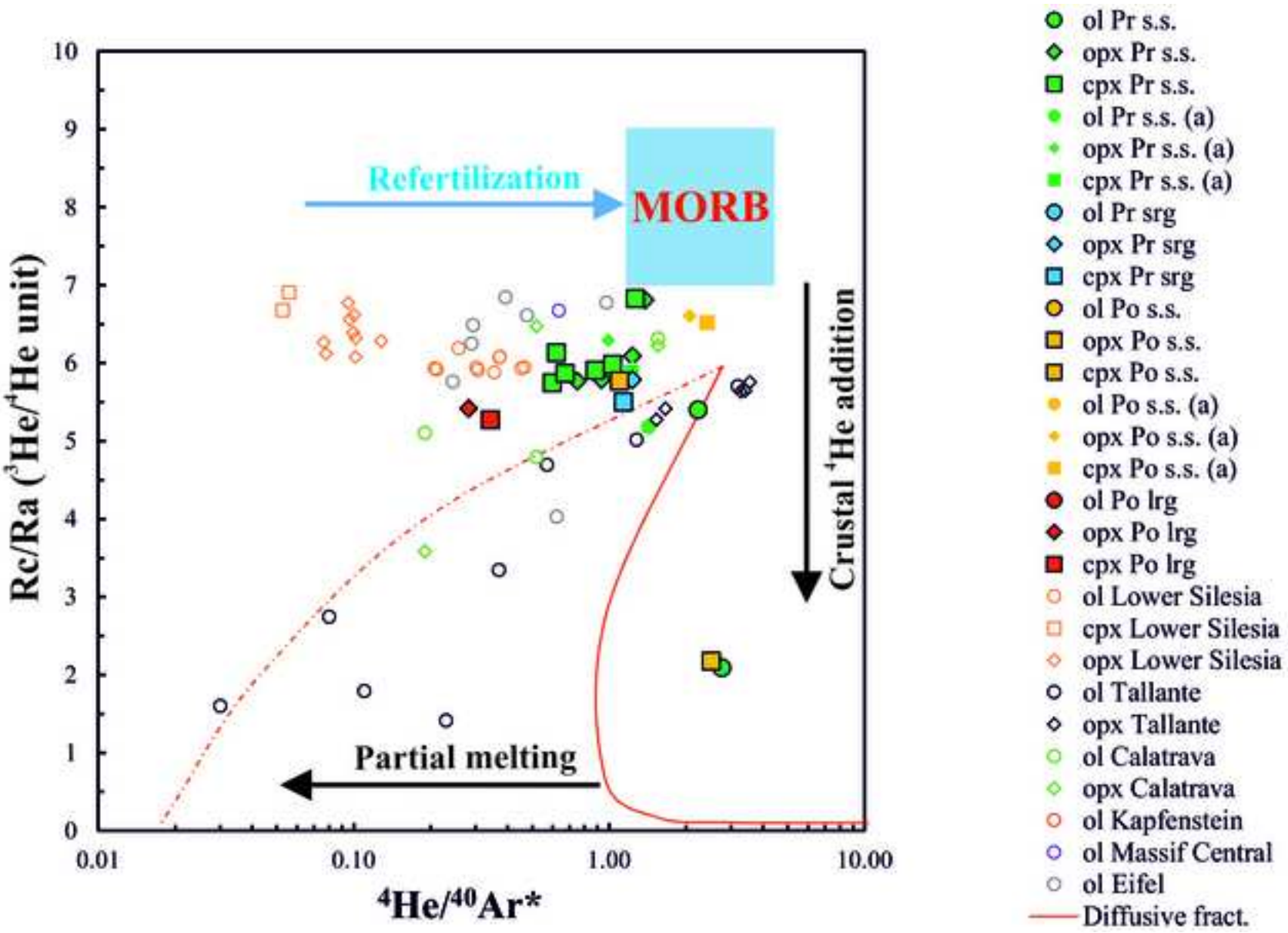

Figure 13

Click here to download high resolution image

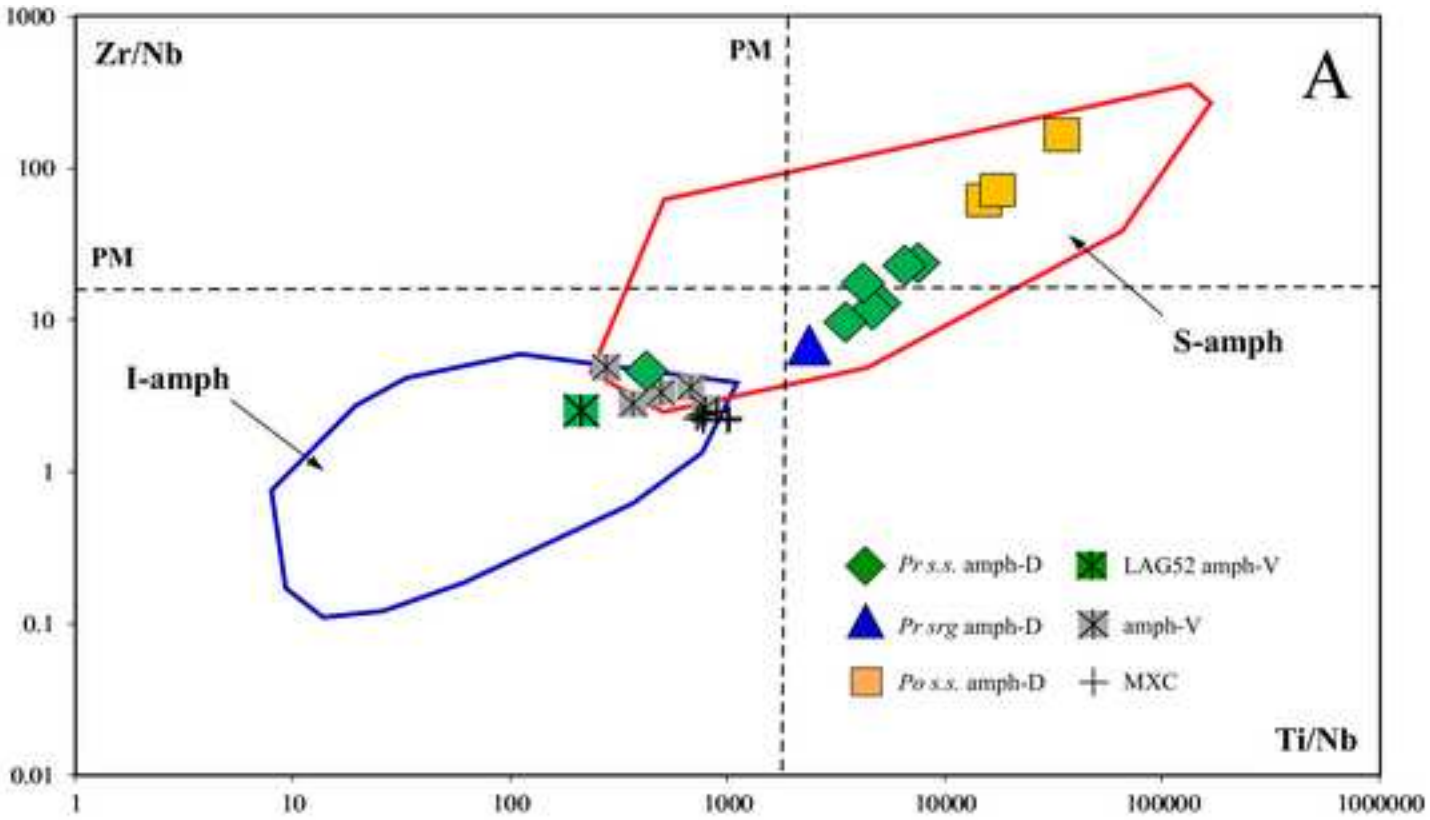

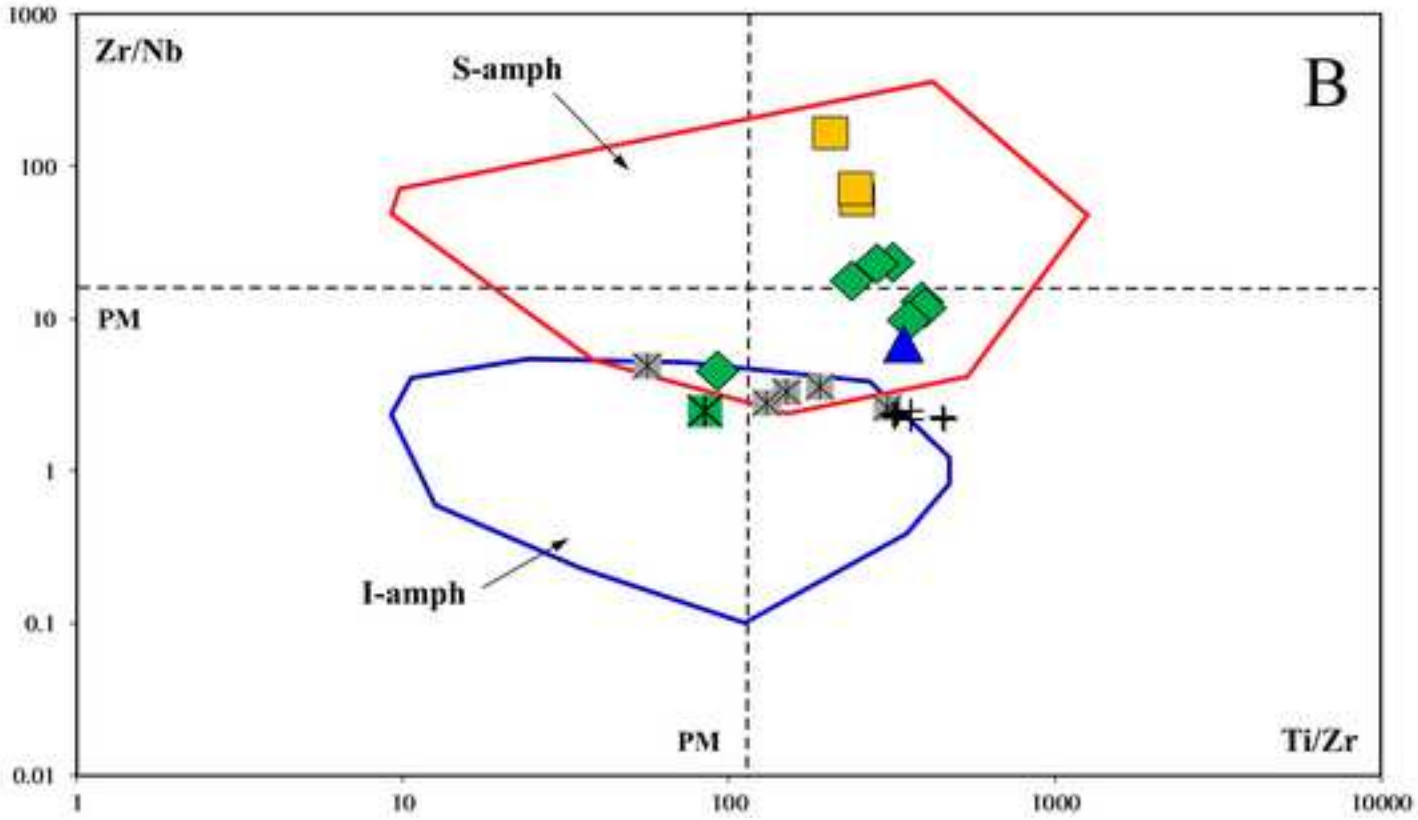

Figure 14

Click here to download high resolution image

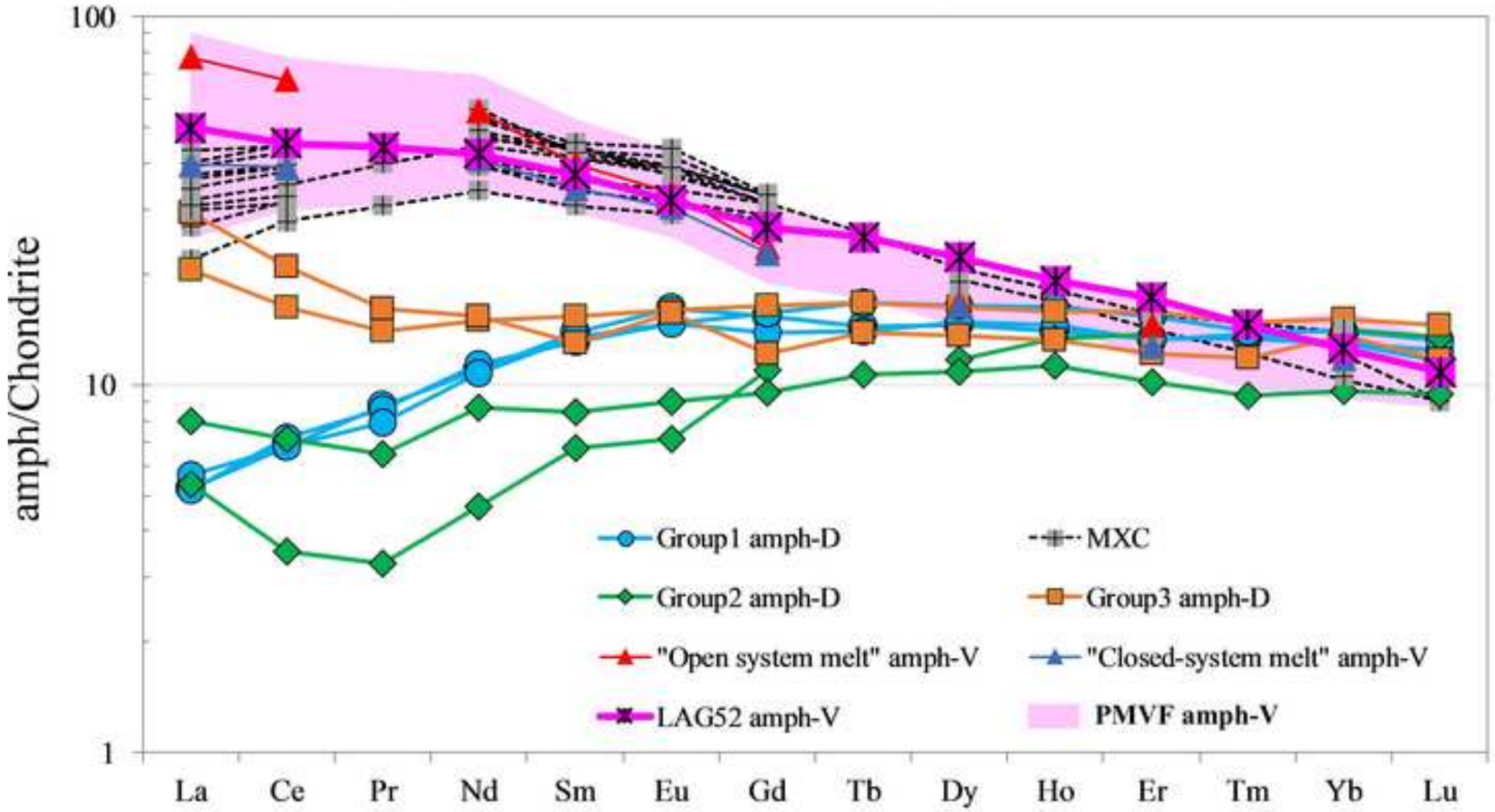

Figure 15

Click here to download high resolution image

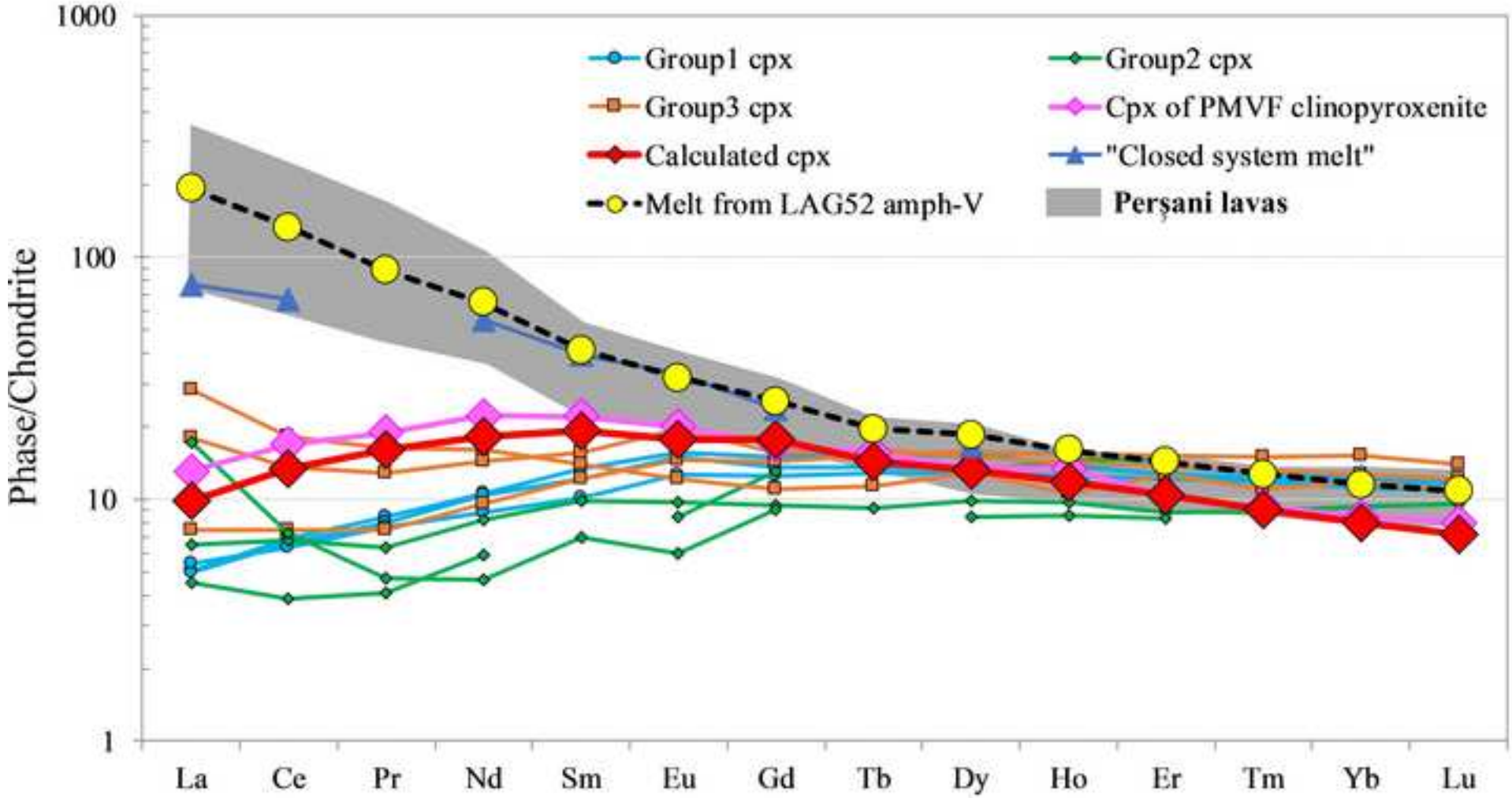

Table 1

Click here to download Table: Table 1.docx

Table 1: Petrographic description, main average petrological data, temperature-pressure-fO_2 estimates and modes for the analyzed PMVF mantle xenoliths. See text for further explanations and model references.

SAMPLE	TEXT. GROUP	Sub-group	ROCK TYPE	fo	cr#	T (°C)* BK	T (°C)* Taylor	T (°C)* O'N&W	P (GPa)§	fO_2	MODAL ABUNDANCES (WT%)				
											ol	opx	cpx	sp	amph
BARQ 4	Protogranular	*Pr s.s.*	Lh	89.9 ±0.12	8.93 ±0.09	1056 ±5.9	1009 ±5.4	1027 ±2.0		- 0.60 ±0.47	56.2	23.6	17.0	3.2	0.0
LAG 2	Protogranular	*Pr s.s.*	Lh(a)	90.5 ±0.03	13 ±0.57	1048 ±0.7	1003 ±12	1003 ±3.4	2.7 ±0.05	0.05 ±0.08	62.2	21.8	11.0	4.0	1.0
LAG 21	Protogranular	*Pr s.s.*	Lh(a)	89.7 ±0.17	12 ±2.12	1018 ±12	989 ±12	1017	2.6 ±0.05	-0.02	58.8	21.0	14.2	5.3	0.7
LAG 24	Protogranular	*Pr s.s.*	Lh(a)	89.8 ±0.11	9.48 ±0.22	1036 ±6.6	984 ±0.6	989 ±8.1	2.7 ±0.05	- 0.78 ±0.11	61.8	22.7	12.7	1.8	1.0
LAG 51	Protogranular	*Pr s.s.*	Lh(a)	90.3 ±0.31	9.91 ±0.42	1023 ±14	997 ±11	1022 ±45	2.5 ±0.05	0.34 ±0.48	60.8	21.6	12.1	3.1	2.4
LAG 52	Protogranular	*Pr s.s.*	Lh(a)	89.3 ±0.20	15.8 ±1.50	992 ±6.7	978 ±12	958 ±16	2.7 ±0.07	0.13 ±0.24	59.6	26.3	8.1	2.0	4.0
TRE 2	Protogranular	*Pr s.s.*	Lh(a)	90.7 ±0.07	15.5 ±0.49	1008 ±2.3	980 ±2.6	970 ±9.8	2.6 ±0.06	- 0.75 ±0.04	64.6	21.0	12.5	0.8	1.1
LAG 1	Protogranular	*Pr srg*	Lh(a)	89.5 ±0.05	9.73 ±0.22	1010 ±3.5	983 ±0.5	994 ±27	2.7 ±0.08	- 0.35 ±0.12	56.5	17.3	21.9	3.5	0.8
TRE 3	Porphyroclastic	*Po lrg*	Lh(a)	90.0 ±0.04	10.9 ±0.06	970 ±0.7	950 ±3.2	979 ±27	2.8 ±0.03	- 0.23 ±0.12	38.5	37.0	19.5	3.0	2.0
TRE 1	Porphyroclastic	*Po s.s.*	Lh	91.5 ±0.27	31.2 ±2.49	897 ±6.2	890 ±1.7	939 ±12		- 1.22 ±0.30	70.9	25.0	2.8	1.3	0.0
TRE 4	Porphyroclastic	*Po s.s.*	Lh(a)	90.0 ±0.13	9.23 ±2.37	843 ±12	858 ±18	961 ±3.9	2.7 ±0.1	0.24 ±0.35	60.5	27.0	9.3	1.9	3.8

(a) contains amphibole

* temperatures calculated at 2.0 GPa

§ pressure estimated using BK temperature at 2.0 Gpa

BK, Taylor and O'N&W stands forBrey and Köhler (1990), Taylor (1998) and O'Neil and Wall (1987) modified by Ballhaus et al. (1991) thermometers, respectively

± indicates standard deviations on about 4 mineral pairs for the geothermomethers and single minerals for the geobaromether

ESM1

Click here to download Background dataset for online publication only: ESM1_Petrographic description of PMVF xenoliths.pdf

ESM2_1

Click here to download Background dataset for online publication only: ESM2-1_Mineral major elements.xlsx

ESM2_2

Click here to download Background dataset for online publication only: ESM2-2_Mineral trace elements.xlsx

ESM2_3

Click here to download Background dataset for online publication only: ESM2-3_Noble gases.xlsx

ESM3

Click here to download Background dataset for online publication only: ESM3_Additional figures and references.pdf